

Setting new constraints on the age of crustal-scale extensional shear zone (Vivero fault): implications for the evolution of Variscan orogeny in the Iberian massif

Marco A. Lopez-Sánchez · Alberto Marcos · Francisco J. Martínez · Alexander Iriondo · Sergio Llana-Fúnez

Received: 6 June 2014 / Accepted: 29 November 2014 / Published online: 21 December 2014
© Springer-Verlag Berlin Heidelberg 2014

Abstract The Vivero fault is crustal-scale extensional shear zone parallel to the Variscan orogen in the Iberian massif belt with an associated dip-slip movement toward the hinterland. To constrain the timing of the extension accommodated by this structure, we performed zircon U-Pb LA-ICP-MS geochronology in several deformed plutons: some of them emplaced syntectonically. The different crystallization ages obtained indicate that the fault was active at least between 303 ± 2 and 287 ± 3 Ma, implying a minimum tectonic activity of 16 ± 5 Ma along the fault. The onset of the faulting is established to have occurred later than 314 ± 2 Ma. The geochronological data confirm that the Vivero fault postdates the main Variscan deformation events in the NW of the Iberian massif and that the extension direction of the Late Carboniferous–Early Permian crustal-scale extensional shear zones along the Ibero-Armorican Arc was consistently perpendicular to the general arcuate trend of the belt in SW Europe.

Keywords Vivero fault · Variscan orogeny · Late Carboniferous–Early Permian extension · Iberian massif · Ibero-Armorican Arc · U–Pb LA-ICP-MS zircon dating

Introduction

Extensional faults and shear zones are common in most orogenic belts during convergence as well as at the final stages of collision. For example, the South Tibetan Detachment in the Himalayas (e.g., Burchfield et al. 1992; Beaumont et al. 2001; Yin 2006; Mukherjee and Koyi 2010a, b; Mukherjee 2013a, b; Mukherjee et al. 2013), moderates crustal thickening during ongoing convergence assisted by its linkage to a weak partially molten layer at mid crustal depths that prevents the upper crust from supporting lateral loads (e.g., Rutter et al. 2011). The progressive attenuation of convergent forces at the end of the orogeny would favor crustal thinning, in addition to the geometrical effect of extensional structures aided by surface erosion, bringing the thickness of the continental crust back to isostatic equilibrium according to its thermal structure. The role of extensional structures in orogenic belts is therefore that of counteracting the inherent thickening of the crust during plate convergence and collision. In the Variscan Belt of Western Europe, two groups of extensional structures are generally portrayed (Burg et al. 1994; Faure 1995): one Namurian–Westphalian (although also Visean; Escuder Viruete et al. 1998; Pereira et al. 2009) and other Late Carboniferous–Early Permian (regarded as ‘late orogenic’ in the Variscan orogeny). Due to the fragmented exposure of isolated Variscan massifs, the structural features and the age of these structures are essential to establish extensional patterns along the orogen to unravel its tectonic history. In the case of Iberian massif, systematic structural studies accompanied by precise and accurate absolute dating of extensional structures are scarce.

The Vivero fault is a crustal-scale extensional shear zone that outcrops in the Variscan basement of the North-western Iberian Peninsula (Fig. 1) and represents the largest

M. A. Lopez-Sánchez (✉) · A. Marcos · S. Llana-Fúnez
Departamento de Geología, Universidad de Oviedo, C/Jesús Arias de Velasco s/n, 33005 Oviedo, Spain
e-mail: malopez@geol.uniovi.es

F. J. Martínez
Departamento de Geología, Universidad Autónoma de Barcelona, Edificio C., 08193 Bellaterra, Barcelona, Spain

A. Iriondo
Universidad Nacional Autónoma de México, Campus Juriquilla, 76230 Juriquilla, Querétaro, Mexico

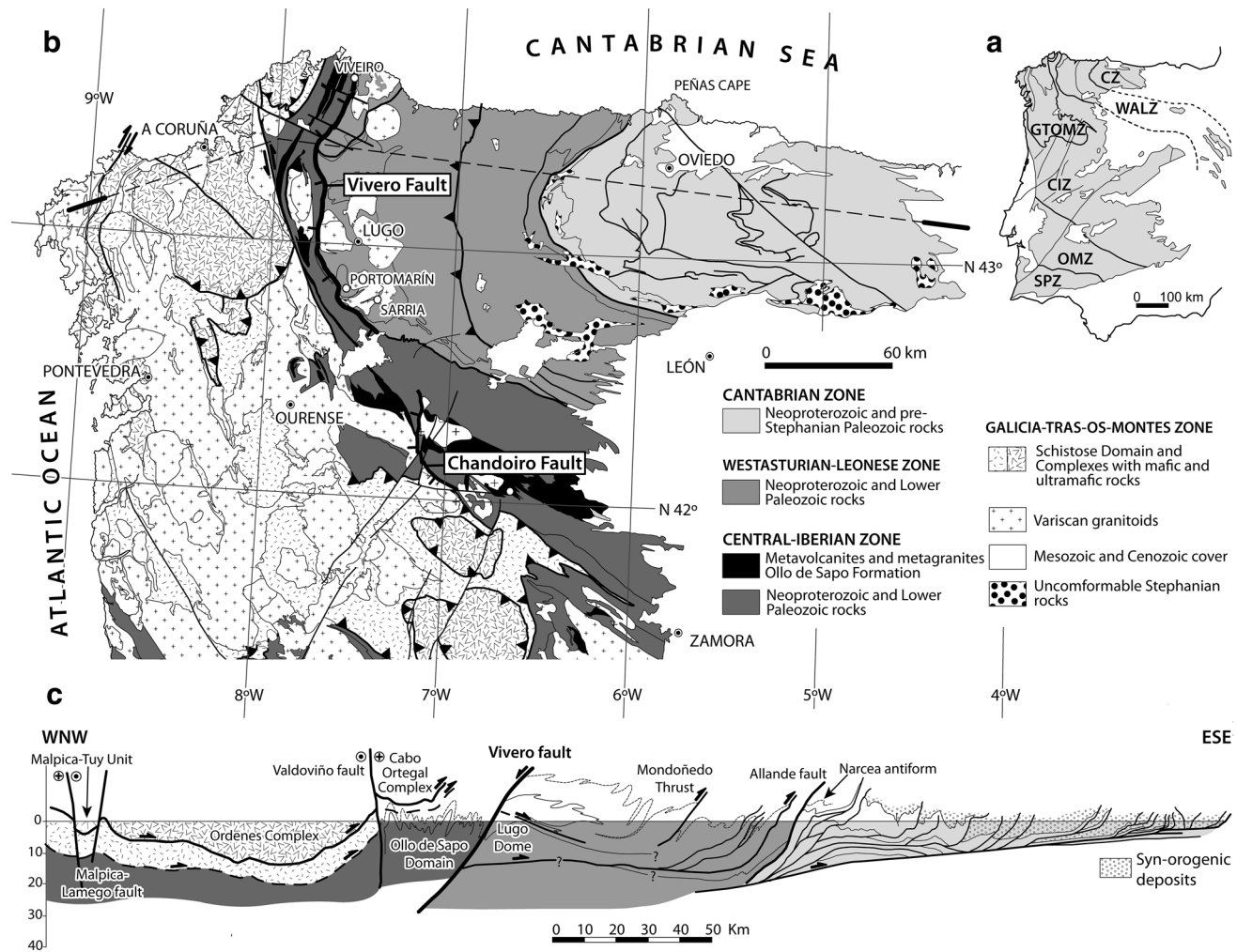


Fig. 1 **a** Iberian massif and zones in which the massif is divided: CZ Cantabrian Zone, WALZ West Asturian-Leonese Zone, GTOMZ Galicia Tras-os-Montes Zone, CIZ Central Iberian Zone, OMZ Ossa Morena Zone, SPZ South Portuguese Zone (Lotze 1945; Julivert et al. 1972; Farias et al. 1987). **b** Simplified geological map of the

northwest Iberian Peninsula (partially based on Parga Pondal et al. 1982; Pérez-Estaún and Bea 2004). **c** General cross section across the northwestern Iberian Variscan belt (partially based on Pérez-Estaún et al. 1991)

normal fault in the hinterland of the NW of Iberian massif. On the basis of the structural, metamorphic and geochronologic data available, different authors have interpreted that the Vivero fault was active at different times during the Variscan orogeny. There is general consensus that the fault postdates a first deformation phase producing the main tectonic fabric in the rock and the tight folding in most parts of the hinterland (Matte 1968; Martínez Catalán 1985; Aranguren and Tubía 1992; Martínez et al. 1996). However, the precise age of the Vivero fault remains unclear.

Available absolute age data to constrain duration of activity along the Vivero fault are limited and mainly based in U-Pb and Pb-Pb zircon and monazite ages performed with ID-TIMS (Isotope dilution-Thermal ionization mass spectrometry) in granitoids deformed by the shear zone related with the Vivero fault (Fernández-Suárez et al. 2000).

The radiometric ages used to constrain tectonic activity involve in many cases plutons with a complex interpretation of their emplacement age. In fact, some of them yield inconsistent zircon and monazite radiometric ages or two different concordia-intercept ages using discordant zircons with different morphologies (Fernández-Suárez et al. 2000). The disparity on the age of the structure is mostly due to some of the dating not being systematic or based on rocks with unclear relation to tectonic activity along the Vivero fault. As an example, contrary to the criteria established in Paterson and Tobisch (1988), it is common practice in previous studies to use the solid-state deformation in plutons geometrically associated with the fault as evidence by itself of a pre-tectonic emplacement of the pluton (i.e., use the radiometric pluton emplacement age as the oldest age limit for the onset of the fault) without considering

other structural and metamorphic relationships (e.g., cleavage-porphyroblast in host rocks).

Our first aim in this contribution is to set new and adequate constrains on the age of the tectonic activity along the Vivero fault using zircon U-Pb LA-ICP-MS (laser ablation inductively coupled plasma mass spectrometry) technique in plutons deformed by the this structure. We consider:

1. To establish timing of pluton emplacement relative to fault related deformation. For this, we combined matrix-porphyroblast relations in host rocks and a detailed structural study at different scales, from microscopic to regional.
2. To evaluate whether previous radiometric ages, if available, are reliable or it is necessary to perform new dating.

Our second aim is to compare the structural features and age of the Vivero fault with other Variscan extensional structures in the Iberian Peninsula and discuss whether the structural pattern and the age of the late orogenic extension in the Iberian massif are comparable to that established in other segments of the Variscan orogen in SW Europe.

Regional geology

The Vivero fault is traceable from the north coast of Spain near Viveiro to the south of Sarria showing a minimum length of 142 km (Fig. 1). It follows the main Variscan structures with an approximately N-S direction and dipping ~60° toward the west (i.e., toward the hinterland). It was first described by Parga Pondal et al. (1967) and with the exception of its southern termination, and the general structure and geometric features of the shear zone are fairly well established since Matte (1968) and Martínez Catalán (1985). The details of the microstructures associated with deformation in the granitoids and host rocks are presented elsewhere (Lopez-Sanchez 2013). The trend of mineral, stretching and magnetic lineations along the fault zone is E-W, excepting in the northernmost segment of the fault, where it shows a WNW (302°) direction (Lopez-Sanchez 2013; see also data in Rathore et al. 1983; Martínez Catalán 1985; Aranguren 1994; Martínez et al. 1996). All kinematic criteria, such as shear bands cleavages in deformed granitoids, asymmetric boudins in footwall rocks and drag folds in the hanging wall rocks, are consistent with a top-to-the-West sense of shear.

The Vivero fault separates two major zones of the Iberian massif with different tectonostratigraphic features: the West Asturian-Leonese Zone at the footwall and the Central Iberian Zone at the hanging wall (Fig. 1). The footwall exposes a metamorphic dome, the Lugo Dome (Capdevila 1969), where the general metamorphic grade is within the

staurolite isograd, locally showing andalusite, sillimanite and migmatites related with the massive intrusion of igneous rocks and overprinting the previous Barrovian-type metamorphism. In the hanging wall, the Ollo de Sapo Domain (Parga Pondal et al. 1964) shows a metamorphic grade mostly within the greenschist facies (Capdevila 1969; González Lodeiro et al. 1981; Bastida et al. 1984). Kyanite-chloritoid-white mica assemblages, which include pseudomorphs of a previous andalusite, were locally developed in high-Al pelites within the Ollo de Sapo Domain (Martínez et al. 1996, 2001; Reche et al. 1998a, b; López-Sánchez 2007) and related with the development of strike-slip shear zones (Martínez et al. 1996; Lopez-Sánchez 2013).

The deformation along the Vivero fault affected the earlier metamorphic Variscan zoning (Barrovian-type) developed during the first stages of the Variscan collision (Capdevila 1969; Martínez and Rôlet 1988; Martínez et al. 1988). Along the adjacent hanging wall rocks of the Vivero fault was described a local metamorphism with staurolite locally evolving to andalusite and biotite-bearing assemblages (Capdevila 1969; Reche et al. 1998a, b; Martínez et al. 2001; Lopez-Sánchez 2013). This metamorphism was superimposed on the previous regional greenschist facies metamorphism, and in some areas also overprints kyanite assemblages similar to those found in the Ollo de Sapo domain related with the strike-slip shear zones. The interpretation of this local metamorphism related with the Vivero fault is controversial. Thus, Reche et al. (1998a, b) and Martínez et al. (2001) consider that the development of kyanite, staurolite and andalusite plus biotite assemblages is related to the activity along the Vivero fault. On the other hand, Arenas and Martínez Catalán (2003) and Martínez Catalán et al. (2003) consider that these assemblages are related with a previous low-dipping extensional shear zone, named “Upper extensional shear zone,” later overprinted by the Vivero fault. An alternative interpretation was point out by Lopez-Sánchez (2013), who considered that the staurolite and andalusite assemblages are syntectonic with the Vivero fault but the kyanite assemblages developed prior to the Vivero fault activity and were later overprinted by them.

Evolution and age of major Variscan structures in the NW of the Iberian massif

The hinterland of the Variscan orogen in NW Iberia shows a series of structures generally grouped into three deformation phases. Some of them are widespread, while others are locally developed despite their significance in the tectonic evolution of the orogenic belt. The development of a continuous foliation S_1 and kilometric sub-vertical to recumbent tight folds with eastward vergence is regarded as the first deformation phase (D1) in the Variscan orogen (Matte 1968; Marcos 1973; Martínez Catalán 1985). The

formation of thrusts and shear zones with tectonic transport to the East that cut the D1 folds connote the second deformation phase (D2) (Ribeiro 1970; Marcos 1971, 1973; Bastida and Pulgar 1978; Martínez Catalán 1985). The major thrusts during D2 emplaced the “allochthonous complexes,” which include suture zone and exotic units, i.e., the tectonic assemblage representing the overthrusting of these oceanic and exotic terranes to the West of Gondwana (Ribeiro 1970). The third deformation phase (D3) explains the development of upright to steeply incline and generally open large folds affecting previous structures and generally producing type 3 interference patterns with the D1 folds (Matte 1968; Marcos 1973; Martínez Catalán 1985). The development of D3 structures across the orogen is heterogeneous and commonly accompanied by the presence of sub-vertical crenulation cleavages or tectonic banding (S3) in domains of previously sub-horizontal anisotropy. In addition to the upright folds, a number of sub-vertical crustal-scale strike-slip shear zones are described in the Central Iberian Zone overprinting previous structures (Iglesias Ponce de León and Choukroune Ponce et al. 1980; Rathore et al. 1983; González Clavijo et al. 1993; Llana-Fúnez and Marcos 2001; Martínez et al. 1996, 2001; Vegas et al. 2001; Lopez-Sánchez 2013). Both the D3 folds and the strike-slip shear zones are compatible with a E–W shortening (in present-day coordinates) and thus have been regarded as structures formed coetaneously under similar geodynamic scenario (e.g., Iglesias Ponce de León and Choukroune Ponce et al. 1980; Llana-Fúnez and Marcos 2007). Other hinterland structures omitting part of the rock sequence, condensing metamorphism or producing a jump in metamorphic evolution zones are regarded as extensional by most authors. Some of them regarded these structures as coetaneous with thrusting or nucleated soon after crustal thickening (Díez Balda et al. 1995; Escuder Viruete et al. 1994, 1998; Escuder Viruete 1998; Martín-González 2007; Alcock et al. 2009), others are considered them late-Vari-scan structures (Matte 1968; Iglesias Ponce de León and Varea Nieto 1982; Hernández Enrile 1991; Macaya et al. 1991; Doblas et al. 1994; Román-Berdiel et al. 1995).

The Variscan orogeny in SW Europe has an arcuate geometry, with the foreland constituting the core of the arc (Matte and Ribeiro 1975). The structures associated with the closure of the Ibero-Armorican Arc are well documented at its core through the study of surface geology (e.g., Julivert and Marcos 1973; Pérez-Estáun et al. 1988) and more recently through systematic paleomagnetic studies (e.g., Weil et al. 2010). However, constraints to the closure of the arc and its effect on the outer part of the arc, the hinterland of the orogen, are less well known. Earlier reviews of the structural development of the orogen related the Ibero-Armorican Arc with the indentation of Gondwana toward microplates involved in the collision (Matte

1986). The stretching lineation along the orogen, pervasive in most parts of the hinterland, was related with the stretching in the hinterland associated with the indentation at an early stage in the collision (Llana-Fúnez and Marcos 2002, 2007). More recently, the arcuate shape was related to a late orogenic folding or an orocline, and the scarce magmatism at the core with the removal and foundering of a lithospheric root by delamination (Gutiérrez-Alonso et al. 2011).

The absolute age of deformation structures described above are far from being accurately established (see Martínez Catalán et al. 2007). So far, the available isotopic data indicates that the S₁ foliation estimated using Ar–Ar whole-rock geochronology ranges between the c. 359 Ma (Devonian-Carboniferous boundary) in the Central Iberian Zone and c. 336 Ma (Visean; Middle Mississippian) in the West Asturian-Leonese Zone (Dallmeyer et al. 1997). Ar–Ar whole-rock analysis in D2 shear zones, which includes the emplacement of the “allochthonous complexes” to the West of Gondwana, constrains their ages in the range of c. 343 (CIZ) to c. 321 (WALZ) Ma (Dallmeyer et al. 1997). Upright folding of previous structures (D3) preceded the deposition of Upper Westphalian B sediments in the West Asturian-Leonese Zone (e.g., Colchen 1974), which suggests an age previous to c. 315 Ma (Richards 2013).

In the Central Iberian Zone, low-dipping extensional shear zones, such as the Berzosa shear zone was tentatively dated with U–Pb monazite assuming that it was partially active during peak metamorphism at c. 330–320 Ma (i.e., basically Namurian) (Valverde Vaquero et al. 1995; Escuder Viruete et al. 1998), while another extensional structure, the Toledo shear zone, could have been active syn- to post-c. 307 Ma (i.e., syn- to post-Stephanian) (Bea et al. 2006). Scattered Ar–Ar ages in relation to local strike-slip structures indicate tectonic activity at c. 307 Ma (Rodríguez et al. 2003; Gutiérrez-Alonso et al. 2010). Regarding the Cantabrian–Asturian Arc, the core of the Ibero-Armorican Arc, paleomagnetic data indicates that Iberia was stable (i.e., no indication of vertical-axis rotation) at Early Permian times (c. 299 Ma) (Weil et al. 2010). On the other hand, according to Weil et al. (2013) and references therein, existing data suggest that oroclinal development started around 310 Ma. The youngest tectonic activity recorded in rocks from the Cantabrian Zone, at the core of the arc, is Early Permian (c. 299–295 Ma) (Merino-Tomé et al. 2009).

Previous data on the age of the Vivero fault

With respect to structural and metamorphic relations between the footwall and the hanging wall, current knowledge indicates that the Vivero fault postdates D1 structures produced during the E–W shortening in the NW of Iberian

massif (see Parga Pondal et al. 1967; Matte 1968; Martínez Catalán 1985; Bastida et al. 1986; Aranguren and Tubía 1992; Martínez et al. 1996, 2001; Reche et al. 1998a, b; Lopez-Sánchez 2013).

Matte (1968) established that the tectonic foliation developed in the hanging wall rock during faulting overprints two Variscan tectonic foliations, a regional fabric (S_1) and the crenulation associated with upright sub-vertical folds (S_3). Later, Martínez Catalán (1985) re-interpreted the Vivero fault as developed previous to the regional refolding stage (D3). Other landmark studies about the relative age of the Vivero fault were as follows: (1) Aranguren and Tubía (1992), who consider that the Vivero fault started during or soon after the last stages of the emplacement of the Mondoñedo nappe (D2 stage); (2) Martínez et al. (1996), who considered that the Vivero fault developed syn- to post-D3 based on hanging wall overprinting relations and the metamorphic evolution; and (3) Martínez Catalán et al. (2003), who considered that the Vivero fault post-dates the last increments of thrusting and spatially coincides and overprints a previous low-dipping extensional shear zone with the same sense of shear named “Upper extensional shear zone.” They interpreted that the “Upper extensional shear zone” was developed during the emplacement of the Mondoñedo Nappe (D2), although later Alcock et al. (2009) reconsidered its development post-dating thrusting and previously to regional re-folding stage (D3) and wrench tectonics, regarding the Vivero fault as a late post-D3 stage extensional fault. The interpretation of the Vivero fault overprinting a previous high- T low-dipping extensional shear zone has been recently contested by Lopez-Sánchez (2013) based on a new interpretation of porphyroblast-matrix relations and the age of the high- T low- P metamorphism. The latter will also be addressed in this study.

As previously mentioned, the absolute ages available to constrain the activity of the Vivero fault are mainly U–Pb and Pb–Pb zircon and monazite ages in granitoids deformed during shearing and performed with ID-TIMS (Isotope dilution-Thermal ionization mass spectrometry) (Fernández-Suárez et al. 2000). These authors used the age of the deformed Penedo Gordo Massif, dated at c. 317 Ma (zircon U–Pb upper intercept age), to set an upper age limit for the onset of faulting. Recently, this pluton has been shown to be emplaced coevally with the movement along the Vivero fault (Lopez-Sánchez 2013), which invalidates the latter assumption by Fernández-Suárez et al. (2000). Another controversial example is the case of the Hombreiro massif (Fig. 3), regarded by Aranguren and Tubía (1992) as a granite emplaced during the emplacement of the Mondoñedo nappe and later deformed by the Vivero fault, but with an age of emplacement later established at 298 ± 5 Ma (Santos

Zalduegui et al. 1996). This age, if correct, is not consistent with the age of thrusting during D2 and therefore with the overlap between the Mondoñedo Nappe and the first stages of Vivero fault activity as they proposed. Alcock et al. (2009) tentatively constrained the activity along the Vivero fault between c. 300 and 286 ± 6 Ma. The c. 300 Ma constrain comes from the Ar/Ar ages found in the metasediments at the core of the Lugo Dome (Dallmeyer et al. 1997), while the 286 ± 6 Ma (Ortega et al. 2000) comes from a whole-rock Rb–Sr age obtained in the Veiga granodiorite, a pluton that is deformed by an extensional fault, the Chandoiro fault (Iglesias Ponce de León and Varea Nieto 1982; Arias et al. 2002), with similar features to those shown by the Vivero fault. The age of the Veiga massif has been later re-dated using zircon U–Pb LA-ICP-MS and its emplacement age corrected to 302 ± 3 Ma (Gutiérrez-Alonso et al. 2011); which invalidate the constrain. As noted above, most relationships between the emplacement of the plutons and the movement of the Vivero fault are not studied in detail. In fact, available absolute age data are scarce and generally difficult to interpret.

On the other hand, there is a reliable age constrain related to the cessation of the fault activity. Reche et al. (1998a) established an age at c. 269 Ma, based on a K–Ar age on biotite obtained by Ries (1979) in the mylonitic facies of Murás leucogranite outcropping within the footwall deformation zone associated with the fault (Fig. 3).

The cross-cutting relations established in the hanging wall by Matte (1968)—which indicates a late post-D3 development of the fault—have not been challenged, so it remains to be seen how to relate the observations made by Matte to those obtained from the footwall structures and the geochronology studies that for some authors suggest that the Vivero fault began its activity previous to the refolding D3 structures (Aranguren and Tubía 1992; Fernández-Suárez et al. 2000) (i.e., syn-convergence extension).

Sample description

Sample DGP-04 (Penedo Gordo granite)

The Penedo Gordo granite is a deformed pluton outcropping in the hanging wall and with its eastern limit in contact with the footwall of the Vivero fault. The pluton shows a general deformation only observable at the microscopic scale, such as the development of blocky sub-grains, dynamic recrystallization by grain boundary migration in quartz and flame-perthite in K-feldspar (Lopez-Sánchez 2013). In its eastern margin and with a thickness up to several meters, there are mylonites and ultramylonites whose

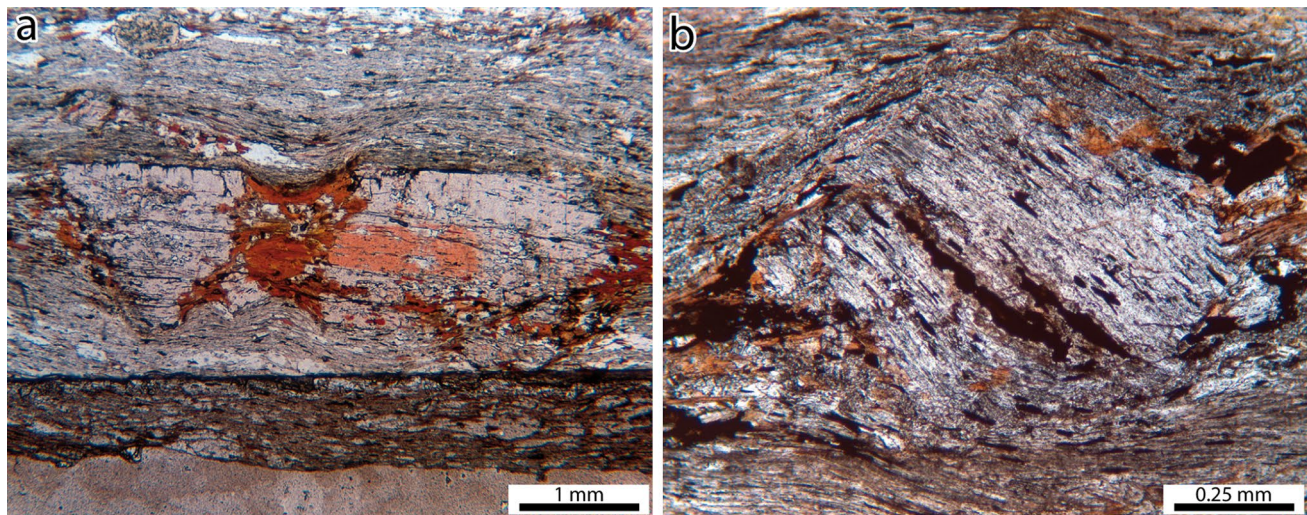


Fig. 2 Matrix-porphyroblast relations within the Vivero fault hanging wall high-strain zone. **a** Andalusite porphyroblast in a garnet-andalusite-biotite-staurolite schist belonging to the Penedo Gordo-Corralvello-Requeixo contact aureole. The andalusite is deformed showing microboudinage. Biotite growing in strain shadows and boudin necks during deformation is indicative of syntectonic growth.

b Andalusite porphyroblast in an andalusite–biotite–staurolite schist belonging to the same contact aureole. Straight inclusions trails inside the andalusite indicate a relative rotation of about 45° with respect to the foliation associated with the Vivero fault. Biotite is present within the asymmetric strain shadows

deformation structures are superimposed on the development of blocky sub-grains (Lopez-Sanchez 2013). The most remarkable feature of this pluton is that the hanging wall host rocks adjacent to the pluton show a metamorphic contact aureole with andalusite porphyroblasts and biotite indicative of syntectonic growth with respect to a tectonic foliation developed during the Vivero fault activity (Lopez-Sanchez 2013) (Fig. 2). The widespread development of blocky sub-grains in quartz is consistent with an early sub-solid-state deformation stage (see Kruhl 1996), subsequently resulting in the strain localization at its eastern margin (Lopez-Sanchez 2013).

Previous radiometric data in this massif provide two different concordia ID-TIMS ages (Fernández-Suárez et al. 2000): an upper intercept age at c. 317 Ma using discordant zircons and interpreted as the granite emplacement age, and a concordia age at 293 ± 2 Ma using two concordant monazites, which could be regarded as related to a separate high- T metamorphic event. Since the zircons obtained in that study were discordant and given the discrepancy between the previous ages obtained from zircon and monazite grains, we considered necessary to confirm the emplacement age with a new dating using LA-ICP-MS technique. The sample was collected in the mylonitic facies of the pluton (Lat-43°35'51,91"N/Long-7°36'37,65"W) (Fig. 3). The emplacement age of this massif indicates the time at which the Vivero fault was indeed active as well as the age of high- T low- P metamorphism with andalusite and biotite developed in adjacent hanging wall rocks.

Sample DGP-05 (Requeixo locality, unnamed mylonitic granite)

This is a mylonitic granite with an S–C fabric indicating top-to-the-West shear. The sample was collected ~4 km S/SW of Penedo Gordo granite (Fig. 3) (Lat-43°31'31,57"N/Long-7°39'46,07"W). The granite follows the contact between the footwall and the hanging wall of the Vivero fault. As in the case of DGP-04, hanging wall rocks show a metamorphic contact aureole with syn-tectonic andalusite and biotite. Therefore, the aim is to date the metamorphic event coeval with the fault movement, allowing the comparison with similar samples (DGP-04 and DGP-06).

Sample DGP-06 (Corralvello locality, unnamed slightly deformed granitic body)

This sample was collected in a decametric fine-grained granitic body located in the hanging wall of the Vivero fault ~6 km S/SW of Penedo Gordo massif (Fig. 3) (Lat-43°30'38,15"N/Long-7°40'36,72"W). This granitic body is enclosed in the hanging wall nodulose schist with andalusite and biotite. As in the case of hanging wall rocks in contact with the Penedo Gordo massif, andalusite and biotite show a contemporary growth with respect to the tectonic foliation associated with the Vivero fault. The aim is to establish the age of the contemporaneous high- T low- P metamorphism and to compare the age of emplacement with those obtained in samples DGP-04 and 05.

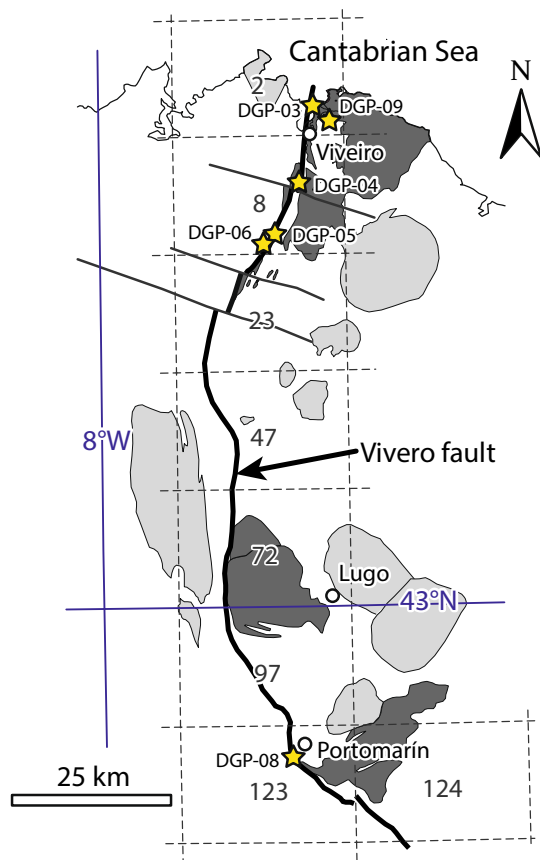


Fig. 3 Simplified geological map showing the Vivero fault, the distribution of plutons around the fault and the sample locations. In dark gray, plutons deformed by the Vivero fault. In light gray, undeformed plutons or without a clear relation with respect to the Vivero fault. The grid corresponds to the boundaries of the Spanish national topographic map at 1:50.000 scale. Sheet numbers are indicated

Sample DGP-03 (Viveiro massif)

The Viveiro massif includes calc-alkaline granitoids and a small volume of ultramafic and mafic rocks (Galán 1987; Galán et al. 1996). The massif is parallel to the Vivero fault and shows in its W margin solid-state deformation structures (S-C' and S-C shear bands) consistent with the movement of the fault (Bastida et al. 1986; Lopez-Sánchez 2013) and affecting the different facies of the massif including the mafic to ultramafic rocks (Galán 1987; Galán et al. 1996).

The monzogranite facies of the massif yielded several concordia ID-TIMS ages (Fernández-Suárez et al. 2000); two intercept ages using discordant zircons with different morphological features at c. 323 (upper intercept) and 315 ± 2 (lower intercept) Ma, respectively, and a concordia age at 295 ± 2 Ma using a concordant monazite. Fernández-Suárez et al. (2000) considered the age of c. 323 Ma as the most probable crystallization age of the monzogranite. A hornblendite belonging to the ultramafic suite was

dated by the same authors using several discordant zircons and a concordant one yielded an upper intercept age of 293 ± 3 Ma.

Because the monzogranite yielded three different radiometric ages, we considered carrying out a new radiometric dating using LA-ICP-MS. The sample was collected in the mylonitic facies of the monzogranite (Lat- $43^{\circ}42'26,38''N$ /Long- $7^{\circ}34'48,32''W$) (Fig. 3). Since the only observable relationship between the pluton and the deformation zone associated with the Vivero fault is the solid-state deformation structures developed in the monzogranite, the emplacement age by itself only predates the cessation of tectonic activity along the Vivero fault.

Sample DGP-09 (deformed granite dykes; San Ciprián massif)

This sample was collected in a quarry located about 3.7 km northeast of Viveiro near the N-642 road (Lat- $43^{\circ}41'06.45''N$ /Long- $7^{\circ}33'29.85''W$). It is a fresh, medium-grained leucocratic granite dyke with a variable thickness of about 30–50 cm. The dyke cuts the gneissic foliation of the finely layered leucocratic gneiss host rocks and it is folded. The dyke appears to be a medium-grained facies of the San Ciprián granite, which presumably is the youngest granite in the zone (see Fernández-Suárez et al. 2000).

There were two previous attempts to set the crystallization age of the San Ciprián pluton: (1) a whole-rock Rb–Sr data that yielded an age of 287 ± 7 Ma (MSWD = 0.52) (Bellido et al. 1992), and (2) U–Pb isotope dilution-thermal ionization mass spectrometry (ID-TIMS) age based on two slightly reverse discordant monazite analyses that yielded a ^{207}Pb - ^{235}U age of 286 ± 2 Ma (Fernández-Suárez et al. 2000). Because whole-rock Rb–Sr and monazite U–Pb ages might represent high temperature metamorphic events, we decided to conduct zircon U–Pb microanalysis to obtain a robust crystallization age. Previous attempt to date this pluton using zircon multi-grain ID-TIMS analyses (Fernández-Suárez et al. 2000) resulted in highly discordant data points due to the presence of major inherited components. Hence, our study used LA-ICP-MS techniques in order to avoid the possibility of inherited cores in many zircons from the San Ciprián pluton. As in the case of the Viveiro massif, the only observable relationship between the pluton and the deformation zone associated with the Vivero fault is the solid-state deformation structures (see also Bastida et al. 1986). Hence, the emplacement age of the pluton by itself only predates the cessation of tectonic activity along the Vivero fault.

Sample DGP-08 (boudinaged granite dykes; Sarria massif)

The sample was collected at the footwall of the Vivero fault in a granitic boudinaged dyke spatially related with

the Sarria massif (Martínez Catalán 1983; Bastida et al. 1986) (Lat-42°47'27,16"N/Long-7°38'33,58"W) (Fig. 3). The boudins were originally associated with the development of the basal shear zone of the Mondoñedo Nappe (D2, top-to-the-East shear sense) (Martínez Catalán 1983). Recent review of these asymmetric boudinaged structures, based on geometric criteria established in Goscombe and Passchier (2003) and extended in Pamplona and Rodrigues (2010), has led to the conclusion that they are shear-band boudins with geometric features consistent with a top-to-the-West shear sense, that is, consistent with the kinematics of the Vivero fault (Lopez-Sánchez 2013).

Previous radiometric data in the Sarria massif yielded a U–Pb concordia age using two discordant monazites at 313 ± 2 Ma (Fernández-Suárez et al. 2000). Furthermore, in the deformed facies of the Vivero fault, there is an Ar–Ar age on muscovite at 282.2 ± 0.6 Ma (Dallmeyer et al. 1997).

Considering the reinterpretation of boudinaged granite dykes as indicating movement of top-to-the-West, and the marked difference in age obtained in the Sarria massif by U–Pb and Ar–Ar methodologies, we concluded that it was necessary to date the boudinaged granite dykes. Furthermore, since the boudinage structures require a competent layer enclosed in an incompetent matrix, these structures show that the dykes cooled previous to its deformation. Given its pre-tectonic nature, this indicates that the age of the dykes can be used a priori to set an older limit to the onset of tectonic activity along the fault.

Analytical methods

Zircon crystals were separated after rock crushing using conventional heavy liquid and magnetic properties at Centro de Geociencias (UNAM). Zircon standard (Plešovice) plus unknowns were mounted in epoxy resin and polished down to expose the near equatorial section. The mounts were cleaned in distilled water and in 1 N HCl and gold-coated for maximum surface conductivity. Cathodoluminescence (CL) images were performed with a JEOL 5600 instrument (SEM) at Denver University.

The laser ablation inductively coupled plasma mass spectrometry (LA-ICP-MS) U(Th)–Pb analyses were performed on individual zircon grains using the facilities at the Isotopic Studies Laboratory (LEI) at the Universidad Nacional Autónoma de México. The detailed procedures used in this study are described in Solari et al. (2010), but briefly, the ablation system consists of a 193 nm ArF Excimer laser (Resonetics model Resolution M50) connected to a Thermo Scientific X-Series quadrupole spectrometer (ICP-MS). A two-volume ablation cell, where the zircon samples are placed, is filled with He (carrier

gas), which provided an optimum atmosphere condition for the laser ablation process (Horn and Günter 2003) and helps washing the ablated aerosol out of the cell. A short, 30-sec, ablation volatilizes a sample area of approximately 33 μm in diameter to $\sim 25 \mu\text{m}$ in depth. The carrier gas and the ablated product are mixed downstream with Ar, and with a small amount of N₂ that allows an increase in plasma temperature when the sample is admitted to the mass spectrometer. For the closest possible control of the measured Pb/U ratios, and to measure the U and Th concentrations, the experiment started with the analysis of a glass standard NIST SRM 612 (~ 38 ppm U composition), followed by five zircon analyses of the Plešovice standard (337.13 ± 0.37 Ma, U–Pb ID-TIMS age at 2-sigma; Sláma et al. 2008), then five unknowns, and thereafter another zircon standard for each five unknowns; the experiment finished with two analyses of zircon standard and another of NIST SRM 612. This standard-bracketing sequence allows the use of the zircon standard to monitor and correct for the effects of instrumental drift and for down-hole isotopic mass fractionation (Jackson et al. 1992; Gehrels et al. 2008; Solari et al. 2010).

The isotopic data obtained by LA-ICP-MS were reduced using the application *UPb.age* (Solari and Tanner 2011). The ratios were corrected offline for common Pb, using the algebraic approach proposed by Andersen (2002), because of the overwhelming ^{204}Hg interference (^{204}Hg is abundantly present in the Ar gas carrier) on the relatively small ^{204}Pb signal prevented accurate online measurements.

Data were projected to the Tera and Wasserburg (1972) and Wetherill (1956) concordia plots along a model common Pb line based on Stacey and Kramers (1975). All the U (Th)–Pb age data presented in Table 1 were plotted using the software Isoplot/Ex 3.75 (Ludwig 2012).

To calculate the emplacement age of granitoids, the procedure was mostly as follows. First, we discarded the zircons with discordances higher than 3 %. The percentage of discordance is obtained using the equation $100 \times [(age^{207}\text{Pb}/^{235}\text{U}) - (age^{206}\text{Pb}/^{238}\text{U})] / (age^{207}\text{Pb}/^{235}\text{U})$. Second, we discard the inherited ages obtained from xenocrysts or ‘mixture ages’ based on field relationships. As an example, all zircons with Neoproterozoic ages were discarded considering that all the granitoids sampled intrude Early Paleozoic rocks. Third, it was verified if there are one or more discordant single-zircon populations. If there is only one consistent discordant single-zircon population, the concordia age is calculated. In all cases, the MSWD (mean square of weighted deviates) must agree with the Wendt and Carl (1991) criteria to confirm statistical significance of the calculated age. Error ellipse uncertainties are 2-sigma, and the concordia ages are within λ errors. The probability of fit and MSWD values take into account the equivalence and concordance of data. In the case of complex discordant

Table 1 LA-ICP-MS U-Th-Pb data (sample DCP-04) for zircon from the Penedo Gordo massif

Sample ^a	U (ppm)	Th (ppm)	Th/U	Corrected ratios				ρ_{ho}^c	$^{208}\text{Pb}/^{232}\text{Th}^b$	$\pm 1 \text{s}^e$	% disc.
				$^{207}\text{Pb}/^{206}\text{Pb}^b$	$\pm 1 \text{s}^e$	$^{207}\text{Pb}/^{235}\text{U}^b$	$\pm 1 \text{s}^e$				
Zircon_30	413	437	0.94	0.06211	0.00106	0.28748	0.00552	0.03351	0.00030	0.460	0.00407
Zircon_15	296	1,035	3.12	0.05590	0.00106	0.32065	0.00661	0.04159	0.00033	0.390	0.00561
Zircon_23	242	115	0.42	0.05564	0.00089	0.32949	0.00746	0.04289	0.00069	0.710	0.01124
Zircon_22	944	187	0.18	0.06011	0.00090	0.37346	0.00819	0.04480	0.00072	0.730	0.01263
Zircon_34	302	157	0.46	0.05182	0.00083	0.32013	0.00562	0.04481	0.00032	0.410	0.01382
Zircon_19	170	91	0.48	0.05426	0.00098	0.33626	0.00651	0.04496	0.00032	0.360	0.01411
Zircon_32	172	73	0.38	0.05316	0.00112	0.33056	0.00737	0.04503	0.00034	0.350	0.01427
Zircon_11	149	170	1.01	0.05559	0.00106	0.34889	0.00737	0.04553	0.00042	0.430	0.00852
Zircon_13	1,117	246	0.20	0.05305	0.00058	0.33292	0.00459	0.04550	0.00038	0.610	0.01047
Zircon_39	74	62	0.75	0.05534	0.00177	0.34921	0.01159	0.04586	0.00040	0.270	0.01459
Zircon_31	155	97	0.56	0.05490	0.00161	0.34797	0.01171	0.04597	0.00037	0.300	0.01435
Zircon_36	103	76	0.66	0.05298	0.00132	0.33567	0.00882	0.04608	0.00037	0.320	0.01385
Zircon_14	1,947	337	0.15	0.05240	0.00046	0.33421	0.00355	0.04618	0.00028	0.560	0.01423
Zircon_24	1,499	170	0.10	0.05251	0.00053	0.33421	0.00400	0.04611	0.00030	0.540	0.01459
Zircon_33	271	98	0.32	0.05287	0.00090	0.33685	0.00637	0.04613	0.00038	0.440	0.01458
Zircon_20	294	134	0.41	0.05308	0.00074	0.33989	0.00526	0.04638	0.00031	0.430	0.01385
Zircon_40	190	89	0.42	0.05400	0.00081	0.34474	0.00589	0.04632	0.00038	0.480	0.01418
Zircon_7	354	132	0.33	0.05274	0.00079	0.33873	0.00564	0.04655	0.00034	0.440	0.01482
Zircon_9	142	127	0.80	0.05346	0.00112	0.34178	0.00767	0.04648	0.00037	0.360	0.01378
Zircon_17	280	111	0.35	0.05308	0.00085	0.34206	0.00604	0.04666	0.00035	0.420	0.01446
Zircon_10	173	84	0.43	0.05652	0.00119	0.36898	0.00820	0.04720	0.00034	0.320	0.01497
Zircon_35	645	193	0.27	0.05313	0.00058	0.34911	0.00443	0.04760	0.00030	0.510	0.01414
Zircon_12	601	185	0.28	0.05236	0.00068	0.34643	0.00515	0.04797	0.00035	0.490	0.01411
Zircon_29	2,118	490	0.21	0.05591	0.00054	0.36950	0.00450	0.04797	0.00036	0.610	0.01454
Zircon_37	262	130	0.44	0.05355	0.00091	0.35460	0.00663	0.04796	0.00037	0.420	0.01360
Zircon_5	536	156	0.26	0.05219	0.00068	0.34496	0.00521	0.04791	0.00037	0.510	0.01447
Zircon_1	213	101	0.42	0.05281	0.00090	0.34976	0.00647	0.04794	0.00035	0.390	0.01342
Zircon_27	124	83	0.60	0.05130	0.00113	0.34038	0.00803	0.04819	0.00041	0.360	0.01432
Zircon_38	98	88	0.80	0.05588	0.00134	0.37211	0.00967	0.04810	0.00048	0.390	0.01492
Zircon_25	113	56	0.44	0.05391	0.00183	0.35924	0.01343	0.04833	0.00038	0.230	0.01512
Zircon_3	107	85	0.70	0.05133	0.00133	0.34264	0.00981	0.04844	0.00058	0.430	0.01473
Zircon_26	1,540	160	0.09	0.05421	0.00056	0.36379	0.00496	0.04867	0.00033	0.580	0.01521
Zircon_28	170	215	1.13	0.05810	0.00163	0.39341	0.01198	0.04942	0.00059	0.390	0.01027
Zircon_16	513	151	0.26	0.05332	0.00080	0.36453	0.00620	0.04967	0.00040	0.470	0.01340

Table 1 continued

Sample ^a	U (ppm)	Th (ppm)	Th/U	Corrected ratios				Rho ^c	$^{208}\text{Pb}/^{232}\text{Th}$ ^b	$\pm 1\text{ s}^e$	% disc.
				$^{207}\text{Pb}/^{206}\text{Pb}$ ^b	$\pm 1\text{ s}^e$	$^{207}\text{Pb}/^{235}\text{U}$ ^b	$\pm 1\text{ s}^e$				
Zircon_18	162	111	0.61	0.05458	0.00115	0.37753	0.00841	0.04992	0.00037	0.320	0.01470
Zircon_4	360	135	0.33	0.05197	0.00078	0.37179	0.00625	0.05174	0.00039	0.450	0.01463
Zircon_2	157	81	0.46	0.05402	0.00103	0.39711	0.00808	0.05289	0.00039	0.350	0.01405
Zircon_6	446	185	0.37	0.05600	0.00067	0.40930	0.00588	0.05295	0.00042	0.550	0.01447
Zircon_8	157	120	0.68	0.06159	0.00129	0.77270	0.01869	0.09106	0.00109	0.500	0.03280
Sample ^a											
Zircon_30	413	437	0.94	212	2	257	4	678	32	82	1
Zircon_15	296	1,035	3.12	263	2	282	5	448	39	113	3
Zircon_23	242	115	0.42	271	4	289	6	438	31	226	4
Zircon_22	944	187	0.18	283	4	322	6	608	28	254	5
Zircon_34	302	157	0.46	283	2	282	4	277	32	277	4
Zircon_19	170	91	0.48	284	2	294	5	382	38	283	4
Zircon_32	172	73	0.38	284	2	290	6	336	42	286	5
Zircon_11	149	170	1.01	287	3	304	6	436	40	171	9
Zircon_13	1,117	246	0.20	287	2	292	3	331	23	211	7
Zircon_39	74	62	0.75	289	2	304	9	426	62	293	5
Zircon_31	155	97	0.56	290	2	303	9	408	57	288	2
Zircon_36	103	76	0.66	290	2	294	7	328	49	278	5
Zircon_14	1,947	337	0.15	291	2	293	3	303	19	286	4
Zircon_24	1,499	170	0.10	291	2	293	3	308	20	293	5
Zircon_33	271	98	0.32	291	2	295	5	323	34	293	6
Zircon_20	294	134	0.41	292	2	297	4	332	28	278	4
Zircon_40	190	89	0.42	292	2	301	4	371	29	285	5
Zircon_7	354	132	0.33	293	2	296	4	318	30	297	4
Zircon_9	142	127	0.80	293	2	299	6	348	41	277	4
Zircon_17	280	111	0.35	294	2	299	5	332	34	290	4
Zircon_10	173	84	0.43	297	2	319	6	473	44	300	5
Zircon_35	645	193	0.27	300	2	304	3	334	22	284	4
Zircon_12	601	185	0.28	302	2	302	4	301	28	283	4
Zircon_29	2,118	490	0.21	302	2	319	3	449	19	292	6
Zircon_37	262	130	0.44	302	2	308	5	352	34	273	4
Zircon_5	536	156	0.26	302	2	301	4	294	26	290	4

Table 1 continued

Sample ^a	U (ppm)	Th (ppm)	Th/U	Corrected ages (Ma)				$^{208}\text{Pb}/^{232}\text{Th}^{\text{d}}$	$\pm 1\text{s}^{\text{e}}$	Best age (Ma)	$\pm 1\text{s}$
				$^{206}\text{Pb}/^{238}\text{U}^{\text{d}}$	$\pm 1\text{s}^{\text{e}}$	$^{207}\text{Pb}/^{235}\text{U}^{\text{d}}$	$\pm 1\text{s}^{\text{e}}$				
Zircon_1	213	101	0.42	302	2	305	5	321	34	269	5
Zircon_27	124	83	0.60	303	3	297	6	254	44	287	5
Zircon_38	98	88	0.80	303	3	321	7	448	47	299	5
Zircon_25	113	56	0.44	304	2	312	10	367	67	303	2
Zircon_3	107	85	0.70	305	4	299	7	256	52	296	4
Zircon_26	1,540	160	0.09	306	2	315	4	380	20	305	2
Zircon_28	170	215	1.13	311	4	337	9	534	54	207	5
Zircon_16	513	151	0.26	312	2	316	5	342	32	269	5
Zircon_18	162	111	0.61	314	2	325	6	395	44	295	4
Zircon_4	360	135	0.33	325	2	321	5	284	30	294	4
Zircon_2	157	81	0.46	332	2	340	6	372	37	282	5
Zircon_6	446	185	0.37	333	3	348	4	452	23	290	4
Zircon_8	157	120	0.68	562	6	581	11	660	39	652	10

^a Samples analyzed July 2010 on the LEI-UNAM LA-ICP-MS^b Isotopic ratios are corrected relative to Plešovice standard zircon (Sláma et al. 2008)^c Rho is the correlation error between errors in the $^{207}\text{Pb}/^{235}\text{U}$ and $^{206}\text{Pb}/^{238}\text{U}$ ratios^d Radiogenic ratios, corrected for common Pb using the ^{204}Pb -correction method, based on the Stacey and Kramers (1975) model^e 1-Sigma errors

zircon populations, we unmixed them using the Sambridge and Compston approach (1994) implemented in the Isoplot/Ex 3.75 (Ludwig 2012), and then we calculated the concordia ages separately. In the cases where it was not possible to calculate concordia ages, we estimated the weighted average age only considering the concordant and/or slightly discordant (less than 10 %) U–Pb ages. In all cases, we provided the weighted average and intercept ages (if applicable) so that they can be compared with the concordia ages considered.

Results

Sample DGP-04 (mylonitic granite facies of Penedo Gordo massif)

SEM-CL images show that zircons from the sample DGP-04 are mainly euhedral and displaying double-terminated prismatic shapes (Fig. 4b). Most of them show brighter inner cores and dark rims under CL, although some of them show the opposite relationship (see zircon 20 in Fig. 4b). The inner cores commonly display a clear growth zoning. This feature is less common in the dark rims but can be observed occasionally as a faint growth zoning. In some cases, the core zoning is cut by the dark rims (see for example zircon number 33 in Fig. 4b), but this is not the general case. Zircon grains show a moderate to high U-content, between 74 and 2,118 ppm, displaying 85 % of them values below the 645 ppm (Table 1).

We performed a total of 39 analyses, from which we can distinguish two coherent age groups of concordant zircons that cannot be attributed to analytical errors (Fig. 5a). The younger group, which includes measures from both the dark rims and the inner cores (Fig. 4b), yields a concordia age of 292 ± 2 Ma (MSWD = 0.78). The older group yields a concordia age of 303 ± 2 Ma (MSWD = 1.14). Interestingly, there are no significant differences in the zircon morphological features between the two groups considered. The youngest concordia age is consistent within the error with the U–Pb concordia age previously obtained by Fernández-Suárez et al. (2000) in this massif using monazite at 293 ± 2 Ma. Furthermore, this age is similar to those obtained in the samples DGP-05 and DGP-06 (see below).

Considering that no zircons as young as c. 303 Ma can be enclosed in the pre-Westphalian sedimentary rocks within the NW of Iberian massif, it is quite clear that the older group of zircons does not represent xenocrysts but antecrusts (in the sense of Charlier et al. 2005 and Miller et al. 2007). Therefore, the younger group of zircons represents the last and main pulse of magma at c. 292 Ma related with the crystallization of the Penedo Gordo massif (i.e., they are phenocrysts).

Sample DGP-05 (Requeixo locality, mylonitic granite)

SEM-CL images show that zircons from the sample DGP-05 are mainly euhedral and displaying double-terminated prismatic shapes (Fig. 4c). Most of them display a clear growth zoning. Excepting the zircon number 1, with 3,452 ppm of uranium, all zircon grains show a moderate U content between 143 and 631 ppm (Table 2).

We performed 39 analysis. Some inner cores yielded Ediacaran ages and are clearly inherited. Most zircons yield Paleozoic ages, as well as some of the zircon rims that have inherited cores (see for example analysis number 11 in Fig. 4c). From the whole dataset of Paleozoic zircons, there is a group of 14 concordant zircons that form a statistically coherent array of ages yielding a concordia age at 292 ± 2 Ma (MSWD = 1.3) (Fig. 5b) that we consider the age of pluton emplacement.

Sample DGP-06 (Corralvello locality, slightly deformed granitic body)

SEM-CL images show that zircons from the sample DGP-06 are mainly euhedral and displaying double-terminated prismatic shapes (Fig. 4d). They show brighter inner cores and dark rims under CL, with the inner cores commonly displaying a clear growth zoning. Few of them are homogeneous unzoned zircon crystals. All zircon grains show a moderate to high U-content, between 319 and 1,621 ppm, excepting two grains (zircons z3 and z29; see Table 3) that have very high U-content values of 15,051 and 5,374 ppm respectively.

We performed a total of 25 analysis. Most zircon grains in this sample are discordant because the loss of lead (Fig. 5c). Only the three older ones (zircons z9, z18 and z11) are concordant (Fig. 4c). Using these three zircons, we obtain a concordia age of 292 ± 2 Ma (MSWD = 1.6; 2-sigma). A similar concordia lower intercept age at 292 ± 2 Ma (MSWD = 2.0) was obtained using a group of selected concordant and discordant grain zircons (Fig. 5c). We consider the obtained age as that for granite emplacement.

Sample DGP-03 (mylonitic granitoid from Vivero massif)

SEM-CL images show that zircons from the sample DGP-03 are mainly euhedral and displaying double-terminated prismatic shapes (Fig. 4a). Most of them show brighter inner cores and dark rims under CL. The inner cores commonly display a clear growth zoning. This feature is less common in the dark rims but can be observed occasionally as a faint growth zoning. In some cases, the core zoning is cut by the dark rims, implying dissolution and reprecipitation processes during its formation, although this



Fig. 4 Scanning electron microscope-cathodoluminescence (SEM-CL) images of selected dated zircons. Circles and the adjacent numbers represent the spot size and the spot number, respectively. The $^{206}\text{Pb}/^{238}\text{U}$ ages are reported in Ma at the 1-sigma level of precision

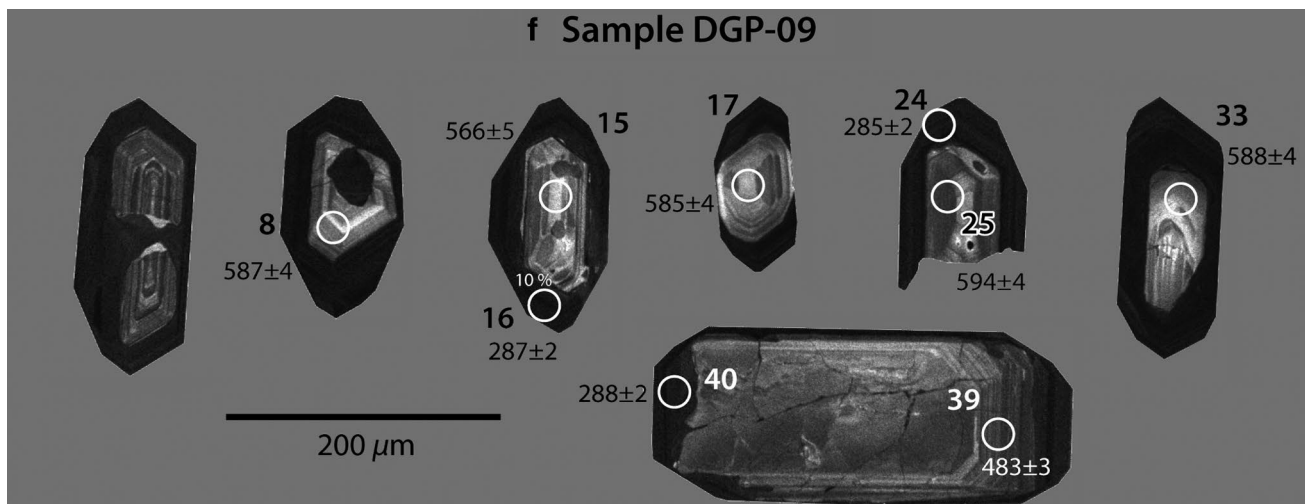


Fig. 4 continued

is not the general case. All zircon grains show a moderate to high U-content, between 297 and 2,352 ppm, with the highest values ($>1,500$ ppm) at the dark-CL rims analyzed (Table 4).

We performed a total of 37 analysis, four of them located at the dark rims of the zircons. Although some bright inner cores yielded Ediacaran ages (Fig. 4a) (i.e., they are xenocrystic cores), there are no significant differences in the Carboniferous dates obtained between the bright inner cores and the dark rims (Fig. 4a; Table 4). From the whole dataset of ages obtained, there is a group of 5 concordant zircons that form a statistically coherent array of ages yielding a concordia age at 314 ± 2 Ma (MSWD = 1.15) (Fig. 5d). This age is inconsistent with the older (zircon, upper intercept age) and the younger (monazite, concordia age) ages previously obtained in this massif with ID-TIMS by Fernández-Suárez et al. (2000), but consistent within the error margins with the lower intercept age at 315 ± 2 Ma discarded by the same authors in support to the oldest one. This coincidence of ages applying two different methods leads us to consider that the most probable age of emplacement for the Vivero monzogranite is 314 ± 2 Ma.

Sample DGP-09 (deformed granite dykes; San Ciprián massif)

SEM-CL images show that zircons are mainly euhedral displaying double-terminated prismatic shapes (Fig. 4f). Almost all grains show brighter cores displaying concentric oscillatory zoning and zoned and/or unzoned dark rims, which in some cases clearly cut the core growth zoning implying dissolution and re-precipitation processes during formation of the rims (Fig. 4f). The bright oscillatory-zoned cores of sample DGP-09 show uranium content

between 173 and 491 ppm (average 333 ppm) (Table 5). In contrast, the U-content in the dark rims is in general one order of magnitude higher, between 867 and 7,166 ppm (Table 5).

We performed a total of 34 analysis, three of them clearly located at the dark rims (numbers 16, 24 and 40) of the zircon (Fig. 4f). Most zircon cores yield Ediacaran ages at about 585 Ma, but there are also zircon groups at c. 565 and c. 548 Ma (Fig. 5e). Only one zircon core yielded a Late Cambrian age at c. 490 Ma (Fig. 5e). These dates clearly indicate that the bright zircon cores are xenocryst. Two of the three dark rims yielded a concordia age at 287 ± 3 Ma (2-sigma, MSWD = 0.89, Prob. of fit = 0.45), similar to the ages previously obtained within the San Ciprián massif. We consider this age to represent the emplacement of the deformed granitic dykes.

Sample DGP-08 (Portomarín locality, boudinaged granite dykes within the Vivero fault)

SEM-CL images show that zircons from the sample DGP-08 display double-terminated prismatic shapes and are significantly smaller compared with the zircons obtained in the other samples studied (Fig. 4e). In contrast with the other zircons studied in this work, they show a patchy appearance under CL (Fig. 4e). The uranium content in these zircons is exceptionally high, being ~75 % of them within the range of 3,000–8,818 ppm and reaching some of them values up to 136,830 ppm (Table 6).

We performed a total of 23 analysis. Most zircon grains in this sample are highly discordant because of a noticeable loss of lead (Fig. 5e). Using one concordant zircon grain (z17) and two slightly discordant grains (z31 and z33, with 8 and 3 % of discordance, respectively), we obtain a

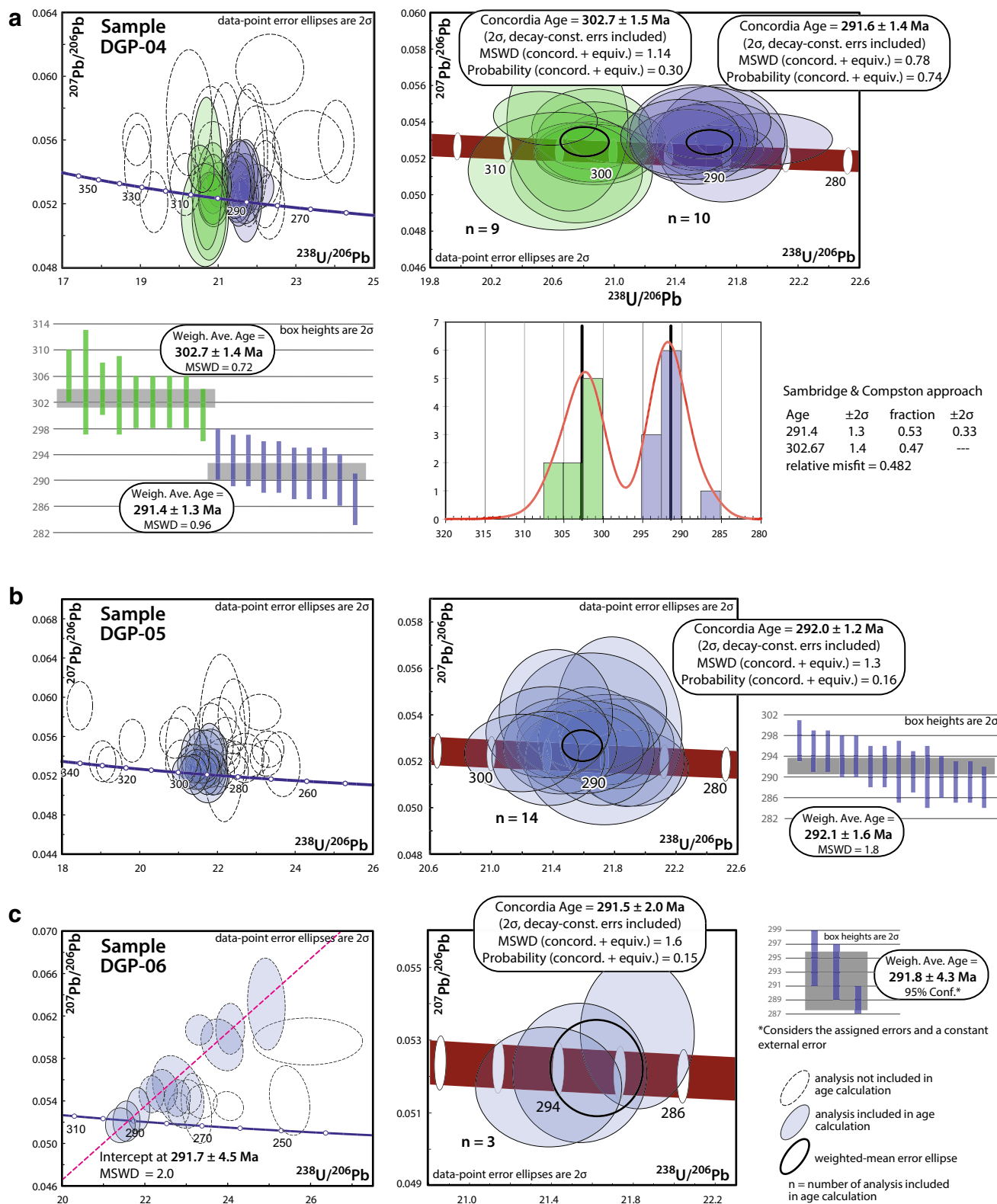


Fig. 5 Concordia and weighted average plots showing the zircon ages of the granitoids dated. All concordia plots are Tera–Wasserburg excepting the concordia plot on the right in (e), which is a Wetherill plot. In weighted average plots, rectangles heights represent the

2-sigma error of the $^{206}\text{Pb}/^{238}\text{U}$ age. In (a), bottom right, it is shown the deconvolution of multiple age components using the Cambridge–Compston approach

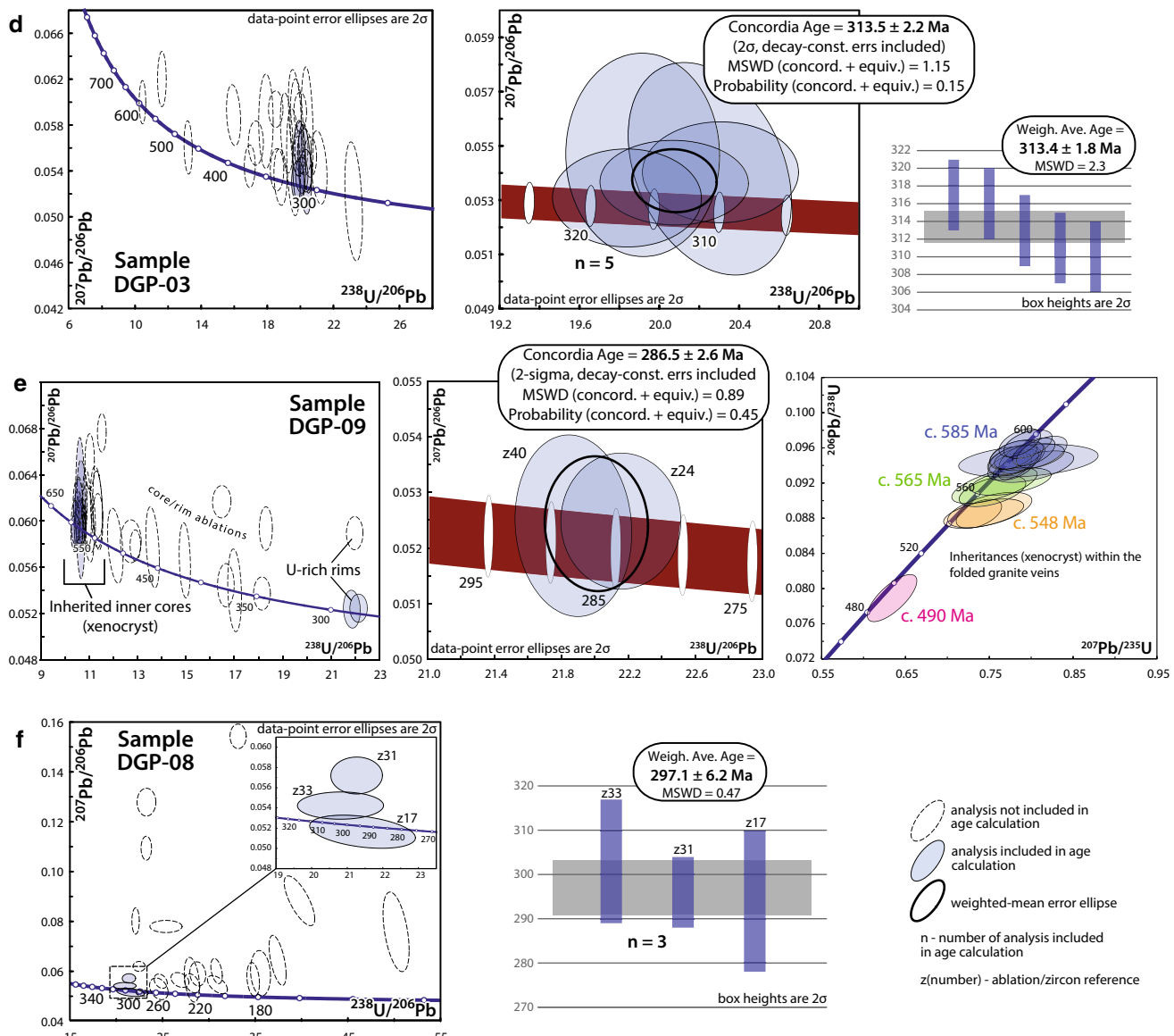


Fig. 5 continued

statistically consistent weighted average age of 297 ± 6 Ma (MSWD = 0.47) (Fig. 5e). This age could represent the emplacement age of granite dykes, but we think it is necessary to take this age with caution since two of the zircon grains used in the age estimation suffer from loss of lead and was not possible to obtain a concordia age.

Discussion

Age constraints

Syn-tectonic emplacement granites in the northern segment of the Vivero fault—samples DGP-04, 05 and

06—yield similar ages and indicate that the fault was active at 292 ± 2 Ma (Figs. 6, 7). Interestingly, these ages are similar to the U-Pb zircon age at 293 ± 3 Ma obtained by Fernández-Suárez et al. (2000) in the deformed ultramafic mantle-derived rocks that outcrop near Vivero (Figs. 6, 7), confirming that these rocks were emplaced and deformed during the movement of the Vivero fault. The ages obtained in the syntectonic granites along the northern segment of the fault are also considered to represent the age of the high- T low- P metamorphism with andalusite plus biotite that locally affects the hanging wall rocks near the Vivero fault in this segment of the fault. The age obtained in the folded granite dykes at 287 ± 3 Ma agrees with the previous proposed crystallization ages for the San Ciprián

Table 2 LA-ICP-MS U-Th-Pb data (sample DCP-05) for zircon from the Requeixo mylonitic granite body

Sample ^a	U (ppm)	Th (ppm)	Th/U	Corrected ratios	$^{207}\text{Pb}/^{206}\text{Pb}^b$	$\pm 1\text{ s}^e$	$^{207}\text{Pb}/^{235}\text{U}^b$	$\pm 1\text{ s}^e$	$^{206}\text{Pb}/^{238}\text{U}^b$	$\pm 1\text{ s}^e$	Rho^c	$^{208}\text{Pb}/^{232}\text{Th}^b$	$\pm 1\text{ s}^e$	% disc.
Zircon_36	325	176	0.49	0.05319	0.00123	0.31038	0.00855	0.04232	0.00036	0.400	0.01326	0.00010	3	
Zircon_13	573	342	0.53	0.05462	0.00076	0.32385	0.00510	0.04292	0.00031	0.470	0.01171	0.00021	5	
Zircon_16	534	507	0.85	0.05386	0.00075	0.31921	0.00503	0.04302	0.00031	0.470	0.01277	0.00019	3	
Zircon_1	3,452	537	0.14	0.05884	0.00076	0.34930	0.00562	0.04330	0.00041	0.600	0.01365	0.00026	10	
Zircon_14	631	490	0.70	0.05359	0.00070	0.32584	0.00576	0.04413	0.00053	0.670	0.01406	0.00025	3	
Zircon_18	504	286	0.51	0.05402	0.00103	0.32713	0.00685	0.04406	0.00039	0.410	0.01362	0.00029	3	
Zircon_34	561	467	0.75	0.05812	0.00157	0.35721	0.01001	0.04462	0.00033	0.270	0.01382	0.00022	9	
Zircon_9	515	252	0.44	0.05365	0.00075	0.33023	0.00510	0.04460	0.00029	0.430	0.01349	0.00022	3	
Zircon_33	439	215	0.44	0.05248	0.00073	0.32396	0.00521	0.04472	0.00035	0.500	0.01363	0.00020	1	
Zircon_29	243	138	0.51	0.05548	0.00100	0.34495	0.00670	0.04503	0.00033	0.370	0.01436	0.00022	6	
Zircon_25	430	177	0.37	0.05392	0.00075	0.33642	0.00544	0.04520	0.00037	0.510	0.01346	0.00022	3	
Zircon_39	496	279	0.50	0.05589	0.00335	0.34845	0.02239	0.04522	0.00050	0.240	0.01408	0.00016	6	
Zircon_24	626	382	0.55	0.05251	0.00068	0.32823	0.00476	0.04529	0.00029	0.450	0.01388	0.00019	1	
Zircon_3	416	249	0.54	0.05738	0.00098	0.36051	0.00679	0.04539	0.00037	0.420	0.01090	0.00016	9	
Zircon_31	328	200	0.55	0.05574	0.00138	0.35102	0.01055	0.04568	0.00043	0.450	0.01423	0.00012	6	
Zircon_38	490	304	0.56	0.05171	0.00067	0.32540	0.00479	0.04563	0.00031	0.470	0.01386	0.00021	-1	
Zircon_2	572	387	0.61	0.05463	0.00087	0.34548	0.00620	0.04585	0.00037	0.460	0.01337	0.00021	4	
Zircon_23	518	256	0.44	0.05372	0.00142	0.33930	0.01010	0.04581	0.00035	0.370	0.01433	0.00010	3	
Zircon_26	487	185	0.34	0.05268	0.00079	0.33351	0.00552	0.04584	0.00032	0.420	0.01408	0.00021	1	
Zircon_19	531	330	0.56	0.05260	0.00068	0.33412	0.00492	0.04603	0.00032	0.480	0.01367	0.00019	1	
Zircon_7	202	83	0.37	0.05215	0.00115	0.33039	0.00794	0.04601	0.00045	0.400	0.01402	0.00027	0	
Zircon_11	386	93	0.22	0.05266	0.00097	0.33495	0.00729	0.04613	0.00033	0.420	0.01447	0.00010	1	
Zircon_21	221	101	0.41	0.05421	0.00103	0.34504	0.00731	0.04620	0.00043	0.440	0.01426	0.00029	3	
Zircon_32	489	197	0.36	0.05238	0.00073	0.33488	0.00537	0.04635	0.00036	0.490	0.01427	0.00021	0	
Zircon_4	586	299	0.46	0.05285	0.00069	0.33807	0.00518	0.04631	0.00038	0.520	0.01426	0.00023	1	
Zircon_20	427	189	0.40	0.05422	0.00114	0.34808	0.00772	0.04670	0.00033	0.320	0.01472	0.00029	3	
Zircon_28	331	96	0.26	0.05260	0.00084	0.33861	0.00593	0.04664	0.00033	0.410	0.01402	0.00027	1	
Zircon_17	359	218	0.55	0.05324	0.00080	0.34385	0.00580	0.04682	0.00036	0.450	0.01466	0.00025	2	
Zircon_22	310	174	0.50	0.05212	0.00083	0.33649	0.00588	0.04681	0.00033	0.410	0.01430	0.00021	0	
Zircon_40	453	248	0.49	0.05230	0.00068	0.34070	0.00506	0.04719	0.00034	0.480	0.01451	0.00022	0	
Zircon_37	166	71	0.38	0.05333	0.00096	0.34917	0.00688	0.04750	0.00038	0.410	0.01499	0.00030	2	
Zircon_8	143	72	0.45	0.05499	0.00159	0.36064	0.01091	0.04740	0.00041	0.290	0.01597	0.00035	4	
Zircon_12	419	131	0.28	0.05593	0.00084	0.36891	0.00622	0.04789	0.00037	0.450	0.01512	0.00024	5	
Zircon_5	252	81	0.29	0.05547	0.00089	0.38766	0.00677	0.05057	0.00035	0.390	0.01934	0.00033	5	

Table 2 continued

Sample ^a	U (ppm)	Th (ppm)	Th/U	Corrected ratios								% disc.
				$^{207}\text{Pb}/^{206}\text{Pb}^b$	$\pm 1\text{ s}^e$	$^{207}\text{Pb}/^{235}\text{U}^b$	$\pm 1\text{ s}^e$	$^{206}\text{Pb}/^{238}\text{U}^b$	$\pm 1\text{ s}^e$	Rho^c	$^{208}\text{Pb}/^{232}\text{Th}^b$	$\pm 1\text{ s}^e$
Zircon_27	377	174	0.42	0.05311	0.00074	0.38211	0.00600	0.05214	0.00037	0.460	0.01559	0.00023
Zircon_35	290	109	0.34	0.05352	0.00086	0.38803	0.00686	0.05260	0.00039	0.420	0.01495	0.00027
Zircon_30	315	52	0.15	0.05930	0.00101	0.44291	0.00821	0.05429	0.00040	0.390	0.02684	0.00072
Zircon_15	264	49	0.17	0.06504	0.00104	1.10290	0.01922	0.12306	0.00085	0.400	0.03691	0.00059
Zircon_10	256	175	0.61	0.06949	0.00083	1.35630	0.01912	0.14121	0.00104	0.530	0.04703	0.00071
Sample ^a												
	U (ppm)	Th (ppm)	Th/U	Corrected ages (Ma)								
Zircon_36	325	176	0.49	267	2	274	7	337	47	266	2	267
Zircon_13	573	342	0.53	271	2	285	4	397	28	235	4	271
Zircon_16	534	507	0.85	272	2	281	4	365	28	256	4	272
Zircon_1	3,452	537	0.14	273	3	304	4	561	25	274	5	273
Zircon_14	631	490	0.70	278	3	286	4	354	26	282	5	278
Zircon_18	504	286	0.51	278	2	287	5	372	38	273	6	278
Zircon_34	561	467	0.75	281	2	310	7	534	53	277	4	281
Zircon_9	515	252	0.44	281	2	290	4	356	28	271	4	281
Zircon_33	439	215	0.44	282	2	285	4	306	28	274	4	282
Zircon_29	243	138	0.51	284	2	301	5	432	36	288	4	284
Zircon_25	430	177	0.37	285	2	294	4	368	28	270	4	285
Zircon_39	496	279	0.50	285	3	304	17	448	118	283	3	285
Zircon_24	626	382	0.55	286	2	288	4	308	26	279	4	286
Zircon_3	416	249	0.54	286	2	313	5	506	33	219	3	286
Zircon_31	328	200	0.55	288	3	305	8	442	49	286	2	288
Zircon_38	490	304	0.56	288	2	286	4	273	26	278	4	288
Zircon_2	572	387	0.61	289	2	301	5	397	32	268	4	289
Zircon_23	518	256	0.44	289	2	297	8	359	53	288	2	289
Zircon_26	487	185	0.34	289	2	292	4	315	30	283	4	289
Zircon_19	531	330	0.56	290	2	293	4	312	26	274	4	290
Zircon_7	202	83	0.37	290	3	290	6	292	45	281	5	290
Zircon_11	386	93	0.22	291	2	293	6	314	42	290	2	291
Zircon_21	221	101	0.41	291	3	301	6	380	38	286	6	291
Zircon_32	489	197	0.36	292	2	293	4	302	28	286	4	292
Zircon_4	586	299	0.46	292	2	296	4	322	26	286	5	292
Zircon_20	427	189	0.40	294	2	303	6	380	42	295	6	294

Table 2 continued

Sample ^a	U (ppm)	Th (ppm)	Th/U	Corrected ages (MA)				$^{208}\text{Pb}/^{232}\text{Th}^d$	$\pm 1\text{s}^e$	Best age (Ma)	$\pm 1\text{s}$
				$^{206}\text{Pb}/^{238}\text{U}$	$\text{d} \pm 1\text{s}^e$	$^{207}\text{Pb}/^{235}\text{U}$	$\text{d} \pm 1\text{s}^e$				
Zircon_28	331	96	0.26	294	2	296	4	312	32	281	5
Zircon_17	359	218	0.55	295	2	300	4	339	30	294	5
Zircon_22	310	174	0.50	295	2	295	4	291	32	287	4
Zircon_40	453	248	0.49	297	2	298	4	299	26	291	4
Zircon_37	166	71	0.38	299	2	304	5	343	36	301	6
Zircon_8	143	72	0.45	299	3	313	8	412	58	320	7
Zircon_12	419	131	0.28	302	2	319	5	450	34	303	5
Zircon_5	252	81	0.29	318	2	333	5	431	32	387	7
Zircon_27	377	174	0.42	328	2	329	4	333	28	313	5
Zircon_35	290	109	0.34	330	2	333	5	351	32	300	5
Zircon_30	315	52	0.15	341	2	372	6	578	33	535	14
Zircon_15	264	49	0.17	748	5	755	9	776	30	733	12
Zircon_10	256	175	0.61	852	6	870	8	913	25	929	14

^a Samples analyzed July 2010 on the LEI-UNAM LA-ICP-MS^b Isotopic ratios are corrected relative to Plešovice standard zircon (Sláma et al. 2008)^c Rho is the correlation error between errors in the $^{207}\text{Pb}/^{235}\text{U}$ and $^{206}\text{Pb}/^{238}\text{U}$ ratios^d Radiogenic ratios, corrected for common Pb using the ^{204}Pb -correction method, based on the Stacey and Kramers (1975) model^e 1-Sigma errors

Table 3 LA-ICP-MS U-Th-Pb data (sample DCP-06) for zircon from the Corralvello deformed granite body

Sample ^a	U (ppm)	Th (ppm)	Th/U	Corrected ratios				$^{208}\text{Pb}/^{232}\text{Th}$ ^b	$\pm 1\text{ s}^{\text{e}}$	% disc.					
				$^{207}\text{Pb}/^{206}\text{Pb}$ ^b	$\pm 1\text{ s}^{\text{e}}$	$^{207}\text{Pb}/^{235}\text{U}$ ^b	$\pm 1\text{ s}^{\text{e}}$								
Zircon_27	429	464	0.97	0.06986	0.001119	0.26207	0.00509	0.02733	0.00026	0.480	0.00485	0.00010	26		
Zircon_6	1,621	234	0.13	0.05984	0.00173	0.22760	0.00889	0.02759	0.00048	0.790	0.00852	0.00016	16		
Zircon_15	477	205	0.39	0.06209	0.00125	0.27835	0.00730	0.03251	0.00033	0.570	0.01000	0.00009	17		
Zircon_10	915	551	0.54	0.05978	0.00090	0.31698	0.00818	0.03855	0.00081	0.810	0.00984	0.00021	13		
Zircon_24	724	285	0.35	0.05405	0.00127	0.29229	0.00802	0.03922	0.00031	0.460	0.01226	0.00009	5		
Zircon_8	1,080	473	0.39	0.06316	0.00168	0.34929	0.01032	0.04011	0.00030	0.320	0.01231	0.00009	16		
Zircon_16	388	95	0.22	0.06100	0.00098	0.34863	0.00596	0.04157	0.00025	0.340	0.01808	0.00034	13		
Zircon_3	15,051	1,587	0.09	0.05354	0.00054	0.30748	0.00394	0.04165	0.00026	0.590	0.01304	0.00008	3		
Zircon_23	923	207	0.20	0.05931	0.00096	0.34286	0.00713	0.04192	0.00037	0.620	0.01296	0.00011	11		
Zircon_17	529	299	0.51	0.05403	0.00065	0.31854	0.00435	0.04280	0.00028	0.470	0.01273	0.00019	4		
Zircon_29	5,374	1,022	0.17	0.06067	0.00058	0.35934	0.00403	0.04292	0.00025	0.520	0.01141	0.00018	13		
Zircon_20	1,092	469	0.39	0.08284	0.01141	0.48954	0.01048	0.04290	0.00056	0.610	0.00999	0.00037	33		
Zircon_28	927	680	0.66	0.05332	0.00127	0.31646	0.00880	0.04305	0.00028	0.490	0.01348	0.00008	3		
Zircon_22	734	503	0.62	0.05452	0.00065	0.32612	0.00438	0.04345	0.00026	0.460	0.01380	0.00019	5		
Zircon_14	607	463	0.69	0.05333	0.00064	0.32206	0.00417	0.04387	0.00021	0.380	0.01358	0.00019	2		
Zircon_2	613	517	0.76	0.05438	0.00071	0.32880	0.00467	0.04392	0.00025	0.390	0.01325	0.00019	4		
Zircon_21	606	314	0.47	0.05487	0.00129	0.33197	0.01027	0.04388	0.00049	0.620	0.01369	0.00014	5		
Zircon_7	718	478	0.60	0.05497	0.00082	0.33850	0.00560	0.04466	0.00031	0.430	0.01419	0.00024	5		
Zircon_25	687	262	0.34	0.05474	0.00071	0.34033	0.00480	0.04516	0.00025	0.390	0.01434	0.00020	4		
Zircon_11	512	302	0.53	0.05330	0.00085	0.33626	0.00567	0.04584	0.00024	0.330	0.01411	0.00020	2		
Zircon_18	409	183	0.40	0.05224	0.00078	0.33367	0.00542	0.04644	0.00029	0.390	0.01428	0.00023	0		
Zircon_9	319	273	0.77	0.05183	0.00067	0.33358	0.00489	0.04677	0.00032	0.470	0.01438	0.00020	-1		
Zircon_13	816	335	0.37	0.06192	0.00080	0.47857	0.00721	0.05613	0.00043	0.510	0.02210	0.00033	11		
Zircon_26	351	222	0.57	0.06467	0.00103	0.68232	0.01249	0.07678	0.00068	0.490	0.02758	0.00041	10		
Zircon_1	557	195	0.31	0.05925	0.00065	0.70521	0.00874	0.08616	0.00049	0.470	0.02636	0.00042	2		
Sample ^a				U (ppm)	Th (ppm)	Th/U	Corrected ages (Ma)								
Sample ^a	U (ppm)	Th (ppm)	Th/U	Corrected ages (Ma)				$^{206}\text{Pb}/^{238}\text{U}$ ^d	$\pm 1\text{ s}^{\text{e}}$	$^{207}\text{Pb}/^{235}\text{U}$ ^d	$\pm 1\text{ s}^{\text{e}}$	$^{208}\text{Pb}/^{232}\text{Th}$ ^d	$\pm 1\text{ s}^{\text{e}}$	Best age (Ma)	$\pm 1\text{ s}$
				$^{206}\text{Pb}/^{238}\text{U}$ ^d	$\pm 1\text{ s}^{\text{e}}$	$^{207}\text{Pb}/^{235}\text{U}$ ^d	$\pm 1\text{ s}^{\text{e}}$	$^{207}\text{Pb}/^{206}\text{Pb}$ ^d	$\pm 1\text{ s}^{\text{e}}$	$^{208}\text{Pb}/^{232}\text{Th}$ ^d	$\pm 1\text{ s}^{\text{e}}$	$^{208}\text{Pb}/^{232}\text{Th}$ ^d	$\pm 1\text{ s}^{\text{e}}$		
Zircon_27	429	464	0.97	174	2	236	4	924	35	98	2	174	2		
Zircon_6	1,621	234	0.13	175	3	208	7	598	63	172	3	175	3		
Zircon_15	477	205	0.39	206	2	249	6	677	43	201	2	206	2		
Zircon_10	915	551	0.54	244	5	280	6	596	32	198	4	244	5		
Zircon_24	724	285	0.35	248	2	260	6	373	53	246	2	248	2		
Zircon_8	1,080	473	0.39	254	2	304	8	714	56	247	2	254	2		

Table 3 continued

Sample ^a	U (ppm)	Th (ppm)	Th/U	Corrected ages (Ma)						$\pm 1\text{s}$
				$^{206}\text{Pb}/^{238}\text{U}^{\text{d}}$	$\pm 1\text{s}^{\text{e}}$	$^{207}\text{Pb}/^{235}\text{U}^{\text{d}}$	$\pm 1\text{s}^{\text{e}}$	$^{207}\text{Pb}/^{206}\text{Pb}^{\text{d}}$	$\pm 1\text{s}^{\text{e}}$	
Zircon_16	388	95	0.22	263	2	304	4	639	34	362
Zircon_3	15,051	1,587	0.09	263	2	272	3	352	23	262
Zircon_23	923	207	0.20	265	2	299	5	579	35	260
Zircon_17	529	299	0.51	270	2	281	3	372	27	256
Zircon_29	5,374	1,022	0.17	271	2	312	3	628	20	229
Zircon_20	1,092	469	0.39	271	3	405	7	1,265	33	201
Zircon_28	927	680	0.66	272	2	279	7	342	54	271
Zircon_22	734	503	0.62	274	2	287	3	393	27	277
Zircon_14	607	463	0.69	277	1	283	3	343	27	273
Zircon_2	613	517	0.76	277	2	289	4	387	29	266
Zircon_21	606	314	0.47	277	3	291	8	407	52	275
Zircon_7	718	478	0.60	282	2	296	4	411	33	285
Zircon_25	687	262	0.34	285	2	297	4	402	29	288
Zircon_11	512	302	0.53	289	1	294	4	342	36	283
Zircon_18	409	183	0.40	293	2	292	4	296	34	287
Zircon_9	319	273	0.77	295	2	292	4	278	29	289
Zircon_13	816	335	0.37	352	3	397	5	671	28	442
Zircon_26	351	222	0.57	477	4	528	8	764	33	550
Zircon_1	557	195	0.31	533	3	542	5	576	24	526

^a Samples analyzed July 2010 on the LEI-UNAM LA-ICP-MS^b Isotopic ratios are corrected relative to Plešovice standard zircon (Sláma et al. 2008)^c Rho is the correlation error between errors in the $^{207}\text{Pb}/^{235}\text{U}$ and $^{206}\text{Pb}/^{238}\text{U}$ ratios^d Radiogenic ratios, corrected for common Pb using the ^{204}Pb -correction method, based on the Stacey and Kramers (1975) model^e 1-Sigma errors

Table 4 LA-ICP-MS U-Th-Pb data (sample DCP-03) for zircon from the Viveiro monzogranite

Sample ^a	U (ppm)	Th (ppm)	Th/U	Corrected ratios	$^{207}\text{Pb}/^{206}\text{Pb}^b$	$\pm 1\text{ s}^e$	$^{207}\text{Pb}/^{235}\text{U}^b$	$\pm 1\text{ s}^e$	$^{206}\text{Pb}/^{238}\text{U}^b$	$\pm 1\text{ s}^e$	Rho^c	$^{208}\text{Pb}/^{232}\text{Th}^b$	$\pm 1\text{ s}^e$	% disc.
Zircon_36	494	160	0.29	0.05136	0.00204	0.30501	0.01380	0.04307	0.00041	0.500	0.01355	0.00017	-1	
Zircon_22	1,541	390	0.23	0.05432	0.00128	0.35490	0.01002	0.04738	0.00045	0.570	0.01481	0.00017	3	
Zircon_26	874	279	0.29	0.07383	0.00214	0.48405	0.01485	0.04758	0.00048	0.330	0.02467	0.00128	25	
Zircon_37	794	332	0.38	0.05526	0.00072	0.37025	0.00559	0.04860	0.00037	0.510	0.01541	0.00023	4	
Zircon_25	743	1,032	1.25	0.05761	0.00211	0.38948	0.01613	0.04903	0.00037	0.390	0.01521	0.00009	7	
Zircon_14	1,207	670	0.50	0.06119	0.00110	0.41551	0.00806	0.04925	0.00035	0.380	0.01551	0.00028	12	
Zircon_38	323	174	0.48	0.05402	0.00076	0.36696	0.00592	0.04925	0.00039	0.490	0.01527	0.00023	2	
Zircon_20	842	1218	1.30	0.05981	0.00132	0.40684	0.00951	0.04939	0.00039	0.330	0.01529	0.00024	10	
Zircon_24	521	390	0.67	0.05559	0.00083	0.37936	0.00654	0.04942	0.00042	0.500	0.01485	0.00024	5	
Zircon_7	1,256	905	0.65	0.05417	0.00149	0.36880	0.01222	0.04938	0.00041	0.530	0.01543	0.00010	3	
Zircon_28	590	643	0.98	0.05361	0.00064	0.36857	0.00526	0.04982	0.00038	0.550	0.01482	0.00022	2	
Zircon_29	704	386	0.49	0.06077	0.00097	0.41814	0.00742	0.04972	0.00038	0.440	0.01366	0.00022	12	
Zircon_18	821	839	0.92	0.05615	0.00095	0.38590	0.00725	0.04989	0.00040	0.430	0.01532	0.00025	5	
Zircon_39	1,235	789	0.58	0.05938	0.00071	0.40870	0.00583	0.05008	0.00039	0.550	0.01549	0.00023	9	
Zircon_9	2,005	262	0.12	0.06131	0.00098	0.42354	0.00876	0.05010	0.00044	0.600	0.01543	0.00015	12	
Zircon_2	473	16	0.03	0.05468	0.00153	0.37865	0.01108	0.05022	0.00040	0.280	0.01568	0.00015	3	
Zircon_21	1,104	624	0.51	0.05552	0.00072	0.38346	0.00577	0.05026	0.00038	0.510	0.01579	0.00024	4	
Zircon_5	586	361	0.56	0.05311	0.00074	0.36907	0.00591	0.05042	0.00039	0.490	0.01627	0.00026	1	
Zircon_13	436	349	0.72	0.05784	0.00161	0.40362	0.01309	0.05061	0.00041	0.420	0.01570	0.00011	8	
Zircon_17	732	679	0.84	0.06060	0.00337	0.42259	0.02714	0.05057	0.00065	0.390	0.01560	0.00016	11	
Zircon_16	1,510	859	0.51	0.05885	0.00155	0.41271	0.01324	0.05086	0.00043	0.590	0.01574	0.00012	9	
Zircon_4	720	447	0.56	0.05479	0.00178	0.38640	0.01476	0.05114	0.00045	0.470	0.01596	0.00012	3	
Zircon_3	653	379	0.52	0.06089	0.00259	0.43373	0.02004	0.05166	0.00045	0.290	0.01593	0.00014	11	
Zircon_40	508	481	0.85	0.05982	0.00072	0.42774	0.00668	0.05164	0.00052	0.640	0.01555	0.00025	10	
Zircon_8	749	393	0.47	0.05735	0.00134	0.41316	0.01182	0.05225	0.00042	0.570	0.01622	0.00011	7	
Zircon_6	1,350	148	0.10	0.05349	0.00095	0.39300	0.00866	0.05328	0.00047	0.530	0.01668	0.00015	1	
Zircon_35	382	90	0.21	0.05430	0.00076	0.40208	0.00667	0.05387	0.00048	0.540	0.01624	0.00029	1	
Zircon_1	1,465	1,255	0.77	0.05958	0.00066	0.44323	0.00659	0.05410	0.00054	0.670	0.01579	0.00025	9	
Zircon_12	368	108	0.26	0.05826	0.00169	0.44974	0.01380	0.05588	0.00056	0.330	0.01815	0.00076	7	
Zircon_11	582	180	0.28	0.05661	0.00079	0.45074	0.00803	0.05790	0.00064	0.620	0.01641	0.00030	4	
Zircon_23	662	135	0.18	0.05444	0.00076	0.44422	0.00718	0.05919	0.00048	0.500	0.01654	0.00030	1	
Zircon_15	1,211	159	0.12	0.06249	0.00239	0.53927	0.02334	0.06259	0.00083	0.490	0.01924	0.00044	11	
Zircon_33	2,352	68	0.03	0.05890	0.00106	0.51002	0.01194	0.06280	0.00069	0.640	0.01944	0.00044	6	
Zircon_10	1,055	326	0.28	0.07470	0.00082	0.65925	0.01026	0.06405	0.00070	0.710	0.03955	0.00063	22	
Zircon_34	507	173	0.31	0.08216	0.00143	0.77933	0.01734	0.06882	0.00059	0.540	0.02052	0.00017	27	

Table 4 continued

Sample ^a	U (ppm)	Th (ppm)	Th/U	Corrected ratios									
				$^{207}\text{Pb}/^{206}\text{Pb}^b$	$\pm 1\text{ s}^e$	$^{207}\text{Pb}/^{235}\text{U}^b$	$\pm 1\text{ s}^e$	$^{206}\text{Pb}/^{238}\text{U}^b$	$\pm 1\text{ s}^e$	Rho^c	$^{208}\text{Pb}/^{232}\text{Th}^b$	$\pm 1\text{ s}^e$	% disc.
Zircon_19	558	49	0.08	0.05609	0.00091	0.58804	0.01155	0.07604	0.00059	0.510	0.02367	0.00019	0
Zircon_31	304	200	0.59	0.06206	0.00099	0.74072	0.01382	0.08656	0.00083	0.520	0.02894	0.00046	5
Zircon_30	297	300	0.91	0.06015	0.00078	0.79844	0.01210	0.09646	0.00075	0.520	0.02842	0.00043	0
Sample ^a	U (ppm)	Th (ppm)	Th/U	Corrected ages (Ma)		$^{206}\text{Pb}/^{238}\text{U}^d$	$\pm 1\text{ s}^e$	$^{207}\text{Pb}/^{235}\text{U}^d$	$\pm 1\text{ s}^e$	$^{207}\text{Pb}/^{206}\text{Pb}^d$	$\pm 1\text{ s}^e$	$^{208}\text{Pb}/^{232}\text{Th}^d$	$\pm 1\text{ s}^e$
Zircon_36	494	160	0.29	272	3	270	11	257	88	272	3	272	3
Zircon_22	1,541	390	0.23	298	3	308	8	384	52	297	3	298	3
Zircon_26	874	279	0.29	300	3	401	10	1037	57	493	25	300	3
Zircon_37	794	332	0.38	306	2	320	4	423	28	309	5	306	2
Zircon_25	743	1032	1.25	309	2	334	12	515	79	305	2	309	2
Zircon_14	1,207	670	0.50	310	2	353	6	646	38	311	6	310	2
Zircon_38	323	174	0.48	310	2	317	4	372	30	306	5	310	2
Zircon_20	842	1,218	1.30	311	2	347	7	597	47	307	5	311	2
Zircon_24	521	390	0.67	311	3	327	5	436	32	298	5	311	3
Zircon_7	1,256	905	0.65	311	2	319	9	378	59	310	2	311	2
Zircon_28	590	643	0.98	313	2	319	4	355	26	297	4	313	2
Zircon_29	704	386	0.49	313	2	355	5	631	33	274	4	313	2
Zircon_18	821	839	0.92	314	2	331	5	458	37	307	5	314	2
Zircon_39	1,235	789	0.58	315	2	348	4	581	25	311	5	315	2
Zircon_9	2,005	262	0.12	315	3	359	6	650	33	310	3	315	3
Zircon_2	473	16	0.03	316	2	326	8	399	61	314	3	316	2
Zircon_21	1,104	624	0.51	316	2	330	4	433	28	317	5	316	2
Zircon_5	586	361	0.56	317	2	319	4	333	30	326	5	317	2
Zircon_13	436	349	0.72	318	3	344	9	524	60	315	2	318	3
Zircon_17	732	679	0.84	318	4	358	19	625	115	313	3	318	4
Zircon_16	1,510	859	0.51	320	3	351	10	562	55	316	2	320	3
Zircon_4	720	447	0.56	322	3	332	11	404	70	320	2	322	3
Zircon_3	653	379	0.52	325	3	366	14	635	90	319	3	325	3
Zircon_40	508	481	0.85	325	3	362	5	597	25	312	5	325	3
Zircon_8	749	393	0.47	328	3	351	8	505	49	325	2	328	3
Zircon_6	1350	148	0.10	335	3	337	6	350	38	334	3	335	3
Zircon_35	382	90	0.21	338	3	343	5	384	30	326	6	338	3
Zircon_1	1,465	1,255	0.77	340	3	373	5	588	23	317	5	340	3
Zircon_12	368	108	0.26	351	3	377	10	540	62	364	15	351	3

Table 4 continued

Sample ^a	U (ppm)	Th (ppm)	Th/U	Corrected ages (Ma)			$^{208}\text{Pb}/^{232}\text{Th}^d$			Best age (Ma)	
				$^{206}\text{Pb}/^{238}\text{U}^d$	$\pm 1\text{s}^e$	$^{207}\text{Pb}/^{235}\text{U}^d$	$\pm 1\text{s}^e$	$^{207}\text{Pb}/^{206}\text{Pb}^d$	$\pm 1\text{s}^e$	$^{208}\text{Pb}/^{232}\text{Th}^d$	$\pm 1\text{s}^e$
Zircon_11	582	180	0.28	363	4	378	6	476	30	329	6
Zircon_23	662	135	0.18	371	3	373	5	389	31	332	6
Zircon_15	1,211	159	0.12	391	5	438	15	691	80	385	9
Zircon_33	2,352	68	0.03	393	4	418	8	564	38	389	9
Zircon_10	1,055	326	0.28	400	4	514	6	1,060	22	784	12
Zircon_34	507	173	0.31	429	4	585	10	1,249	33	411	3
Zircon_19	558	49	0.08	472	4	470	7	456	34	473	4
Zircon_31	304	200	0.59	535	5	563	8	676	33	577	9
Zircon_30	297	300	0.91	594	4	596	7	609	27	566	8
										594	4

^a Samples analyzed July 2010 on the LEI-UNAM LA-ICP-MS^b Isotopic ratios are corrected relative to Plešovice standard zircon (Sláma et al. 2008)^c Rho is the correlation error between errors in the $^{207}\text{Pb}/^{235}\text{U}$ and $^{206}\text{Pb}/^{238}\text{U}$ ratios^d Radiogenic ratios, corrected for common Pb using the ^{204}Pb -correction method, based on the Stacey and Kramers (1975) model^e 1-Sigma errors

granite (Bellido et al. 1992; Fernández-Suárez et al. 2000). This result extends the activity of the Vivero fault between c. 292 and the 287 ± 3 Ma and confirms that the emplacement of the San Ciprián granite was concomitant with the development of the Vivero fault.

The Permian ages obtained in the northern segment of the fault are consistent within the error, although slightly younger, with the age of the Hombreiro massif at 298 ± 5 Ma (whole-rock Rb–Sr; Santos Zalduegui et al. 1996) located in the middle segment of the fault (Fig. 7). The sub-solidus deformation microstructures related with the Vivero fault shear zone described in this pluton by Aranguren and Tubía (1992) suggest an emplacement concomitant with the beginning of the fault.

In contrast to the other ages found in this study, the age obtained in the Vivero monzogranite (sample DGP-03) at 314 ± 2 Ma is significantly older (Figs. 5, 6). This age is similar to that previously obtained in the Sarria massif at 313 ± 2 Ma by Fernández-Suárez et al. (2000) and suggests that the emplacement of these middle Pennsylvanian (Westphalian) plutons precedes the activity of the Vivero fault and therefore can be used as a potential older limit for the onset of the faulting activity. Interestingly, the monazites obtained in the Viveiro monzogranite yielded an U–Pb concordant age at 295 ± 2 Ma (Fernández-Suárez et al. 2000), which is consistent with the Early Permian ages obtained in most syntectonic plutons (Figs. 5, 6). We suggest that this age could be consequence of the resetting of the monazite isotopic system related with the magmatism associated with the Vivero fault, including the emplacement of the ultramafic rocks spatially associated with this monzogranite. A similar interpretation with the emplacement of the ultramafic rocks was previously proposed by Fernández-Suárez et al. (2000), but without specific mention to the role of the Vivero fault.

In the southern segment of the fault, we obtained an age of 297 ± 6 Ma in the Portomarín boudinage granite dykes (*sample DGP-08*), which is slightly older, although still consistent within error, compared to those obtained in the northern segment of the fault (Fig. 6). However, as revealed in the results section, this age does not seem totally consistent. Leaving aside the reported loss of lead in zircon grains previously mentioned, the previous U–Pb concordia age of the spatially associated Sarria massif using two monazites, set at 313 ± 2 Ma (Fernández-Suárez et al. 2000), make this date controversial. The age yielded by the monazites, which is clearly older, is only possible if the dykes are not related with the Sarria massif, which presumably seems unlikely. Consequently, we discard the date obtained in the sample DGP-08. In any event, we think it is necessary a further study in the future to set a reliable age of these boudinaged dykes.

Table 5 LA-ICP-MS U-Th-Pb data (sample DCP-09) for zircon from the folded granite dykes belonging to the San Ciprián massif

Sample ^a	Comment	U (ppm)	Th (ppm)	Th/U	Corrected ratios				Rho ^c	$^{208}\text{Pb}/^{232}\text{Th}^b$	$\pm 1 \text{s}^e$	% disc.		
					$^{207}\text{Pb}/^{206}\text{Pb}^b$	$\pm 1 \text{s}^e$	$^{207}\text{Pb}/^{235}\text{U}^b$	$\pm 1 \text{s}^e$						
Zircon_24	Rim, high U	3,175	127	0.04	0.05238	0.00050	0.32670	0.000380	0.04514	0.00030	0.570	0.01619	0.00023	1
Zircon_16	Rim, high U	2,151	60	0.03	0.05885	0.00059	0.36885	0.00439	0.04547	0.00029	0.540	0.04973	0.00109	10
Zircon_40	Rim, high U	1,729	45	0.02	0.05241	0.00070	0.33045	0.00489	0.04573	0.00030	0.510	0.01435	0.00043	1
Zircon_22	Core-rim?	930	84	0.08	0.05912	0.00077	0.44757	0.00645	0.05466	0.00034	0.430	0.03416	0.00051	9
Zircon_29	Core-rim?	725	65	0.08	0.05375	0.00059	0.40876	0.00551	0.05514	0.00043	0.580	0.02659	0.00043	1
Zircon_32	Core-rim?	846	71	0.08	0.05404	0.00148	0.43842	0.01278	0.05884	0.00041	0.410	0.01840	0.00056	0
Zircon_13	Core-rim?	719	31	0.04	0.05448	0.00076	0.45174	0.00735	0.06013	0.00050	0.510	0.02532	0.00076	1
Zircon_36	Core-rim?	1,704	152	0.08	0.06151	0.00057	0.51677	0.00683	0.06073	0.00058	0.710	0.03713	0.00052	10
Zircon_37	Core-rim?	1,176	157	0.12	0.05665	0.00134	0.52354	0.01341	0.06703	0.00043	0.440	0.02084	0.00039	2
Zircon_3	Core-rim?	1,245	192	0.14	0.05775	0.00147	0.58608	0.01694	0.07360	0.00062	0.590	0.02283	0.00051	2
Zircon_39	Core-rim?	1,245	208	0.15	0.05757	0.00055	0.62093	0.00733	0.07774	0.00054	0.590	0.02767	0.00039	1
Zircon_27	Core	318	62	0.18	0.05820	0.00076	0.63412	0.01211	0.07891	0.00110	0.730	0.02877	0.00043	2
Zircon_1	Core-rim?	1001	228	0.21	0.05789	0.00135	0.66359	0.01924	0.08313	0.00092	0.680	0.02578	0.00036	0
Zircon_11	Core	741	196	0.24	0.06756	0.00068	0.81416	0.00967	0.08725	0.00056	0.530	0.03659	0.00051	11
Zircon_19	Core	364	158	0.39	0.06042	0.00079	0.73798	0.01111	0.08848	0.00067	0.500	0.02773	0.00042	2
Zircon_23	core	449	136	0.28	0.06094	0.00136	0.74376	0.01948	0.08852	0.00068	0.540	0.02729	0.00024	3
Zircon_31	Core	298	123	0.38	0.06124	0.00138	0.75081	0.02056	0.08892	0.00083	0.550	0.02740	0.00027	4
Zircon_5	Core	504	217	0.39	0.06007	0.00107	0.75420	0.01631	0.09106	0.00072	0.510	0.02812	0.00022	2
Zircon_6	core	503	239	0.43	0.06490	0.00097	0.81961	0.01375	0.09117	0.00068	0.450	0.02581	0.00075	8
Zircon_15	core	365	142	0.35	0.05983	0.00133	0.75661	0.02085	0.09171	0.00084	0.640	0.02833	0.00024	1
Zircon_38	Core	267	84	0.29	0.06111	0.00137	0.77636	0.01962	0.09215	0.00064	0.490	0.02840	0.00027	3
Zircon_21	Core	378	170	0.41	0.06205	0.00126	0.80306	0.01973	0.09386	0.00073	0.540	0.02887	0.00020	4
Zircon_4	core	449	155	0.31	0.05971	0.00072	0.77483	0.01069	0.09387	0.00064	0.490	0.02847	0.00043	1
Zircon_20	Core	491	164	0.30	0.06047	0.00060	0.78513	0.00977	0.09408	0.00070	0.600	0.02916	0.00044	1
Zircon_2	Core	198	77	0.35	0.06116	0.00238	0.79705	0.03401	0.09452	0.00076	0.320	0.02913	0.00022	2
Zircon_12	Core	236	120	0.46	0.05977	0.00090	0.78026	0.01309	0.09457	0.00071	0.440	0.02818	0.00042	1
Zircon_14	Core	173	48	0.26	0.05972	0.00084	0.77971	0.01231	0.09460	0.00069	0.450	0.02919	0.00061	0
Zircon_35	core	343	110	0.29	0.06029	0.00072	0.78944	0.01126	0.09483	0.00073	0.550	0.02813	0.00045	1
Zircon_17	core	252	89	0.32	0.06095	0.00111	0.79806	0.01702	0.09497	0.00062	0.440	0.02927	0.00018	2
Zircon_9	Core	253	78	0.28	0.05927	0.00077	0.77878	0.01150	0.09519	0.00067	0.480	0.02886	0.00043	0
Zircon_8	Core	308	109	0.32	0.05959	0.00089	0.78288	0.01296	0.09525	0.00067	0.430	0.02915	0.00044	0
Zircon_10	Core	385	115	0.27	0.06091	0.00067	0.80346	0.01039	0.09553	0.00065	0.530	0.02852	0.00043	2
Zircon_33	Core	189	56	0.27	0.06161	0.00080	0.81294	0.01232	0.09551	0.00074	0.520	0.02810	0.00042	3
Zircon_26	Core	244	91	0.34	0.05984	0.00078	0.79655	0.01176	0.09642	0.00067	0.470	0.03325	0.00276	0

Table 5 continued

Sample ^a	Comment	U (ppm)	Th (ppm)	Th/U	Corrected ratios												
					$^{207}\text{Pb}/^{206}\text{Pb}^b$	$\pm 1\text{ s}^e$	$^{207}\text{Pb}/^{235}\text{U}^b$	$\pm 1\text{ s}^e$	$^{206}\text{Pb}/^{238}\text{U}^b$	$\pm 1\text{ s}^e$	$^{207}\text{Pb}/^{206}\text{Pb}^d$	$\pm 1\text{ s}^e$	$^{208}\text{Pb}/^{232}\text{Th}^b$	$\pm 1\text{ s}^e$	Rho ^c	$^{208}\text{Pb}/^{232}\text{Th}^b$	$\pm 1\text{ s}^e$
Zircon_25	Core	343	156	0.41	0.05890	0.00065	0.78667	0.01013	0.09657	0.00065	0.520	0.02881	0.00043	-1			% disc.
Sample ^a	Comment	U (ppm)	Th (ppm)	Th/U	Corrected ages (Ma)												
Zircon_24	Rim, high U	3,175	127	0.04	285	2	287	3	302	22	325	5	285	2			
Zircon_16	Rim, high U	2,151	60	0.03	287	2	320	3	562	21	981	21	287	2			
Zircon_40	Rim, high U	1,729	45	0.02	288	2	290	4	303	30	288	9	288	2			
Zircon_22	Core-rim?	930	84	0.08	343	2	376	5	572	27	679	10	343	2			
Zircon_29	Core-rim?	725	65	0.08	346	3	348	4	361	25	530	8	346	3			
Zircon_32	Core-rim?	846	71	0.08	369	2	369	9	373	62	368	11	369	2			
Zircon_13	Core-rim?	719	31	0.04	376	3	378	5	391	31	505	15	376	3			
Zircon_36	Core-rim?	1,704	152	0.08	380	4	423	5	657	20	737	10	380	4			
Zircon_37	Core-rim?	1,176	157	0.12	418	3	428	9	478	52	417	8	418	3			
Zircon_3	Core-rim?	1,245	192	0.14	458	4	468	11	520	56	456	10	458	4			
Zircon_39	Core-rim?	1,245	208	0.15	483	3	490	5	513	21	552	8	483	3			
Zircon_27	Core	318	62	0.18	490	7	499	8	537	28	573	8	490	7			
Zircon_1	Core-rim?	1,001	228	0.21	515	5	517	12	526	51	514	7	515	5			
Zircon_11	Core	741	196	0.24	539	3	605	5	855	20	726	10	539	3			
Zircon_19	Core	364	158	0.39	547	4	561	6	619	27	553	8	547	4			
Zircon_23	Core	449	136	0.28	547	4	565	11	637	48	544	5	547	4			
Zircon_31	Core	298	123	0.38	549	5	569	12	648	48	546	5	549	5			
Zircon_5	Core	504	217	0.39	562	4	571	9	606	38	560	4	562	4			
Zircon_6	Core	503	239	0.43	562	4	608	8	771	31	515	15	562	4			
Zircon_15	Core	365	142	0.35	566	5	572	12	598	45	565	5	566	5			
Zircon_38	Core	267	84	0.29	568	4	583	11	643	48	566	5	568	4			
Zircon_21	Core	378	170	0.41	578	4	599	11	676	41	575	4	578	4			
Zircon_4	Core	449	155	0.31	578	4	583	6	593	26	567	8	578	4			
Zircon_20	Core	491	164	0.30	580	4	588	6	620	20	581	9	580	4			
Zircon_2	Core	198	77	0.35	582	4	595	19	645	80	580	4	582	4			
Zircon_12	Core	236	120	0.46	583	4	586	7	595	31	562	8	583	4			
Zircon_14	Core	173	48	0.26	583	4	585	7	593	29	582	12	583	4			
Zircon_35	Core	343	110	0.29	584	4	591	6	614	26	561	9	584	4			

Table 5 continued

Sample ^a	Comment	U (ppm)	Th (ppm)	Th/U	Corrected ages (Ma)									
					²⁰⁶ Pb/ ²³⁸ U ^d	$\pm 1\text{s}^e$	²⁰⁷ Pb/ ²³⁵ U ^d	$\pm 1\text{s}^e$	²⁰⁸ Pb/ ²³² Th ^d	$\pm 1\text{s}^e$	Best age (Ma)	$\pm 1\text{s}$		
Zircon_17	Core	252	89	0.32	585	4	596	10	637	37	583	4	585	4
Zircon_9	Core	253	78	0.28	586	4	585	7	577	28	575	8	586	4
Zircon_8	Core	308	109	0.32	587	4	587	7	589	32	581	9	587	4
Zircon_10	Core	385	115	0.27	588	4	599	6	636	22	568	8	588	4
Zircon_33	Core	189	56	0.27	588	4	604	7	661	28	560	8	588	4
Zircon_26	Core	244	91	0.34	593	4	595	7	598	28	661	54	593	4
Zircon_25	Core	343	156	0.41	594	4	589	6	563	24	574	8	594	4

^a Samples analyzed July 2010 on the LEI-UNAM LA-ICP-MS^b Isotopic ratios are corrected relative to Přešovice standard zircon (Sláma et al. 2008)^c Rho is the correlation error between errors in the ²⁰⁷Pb/²³⁵U and ²⁰⁶Pb/²³⁸U ratios^d Radiogenic ratios, corrected for common Pb using the ²⁰⁴Pb-correction method, based on the Stacey and Kramers (1975) model^e 1-Sigma errors

Overall, the previous geochronological data and the data provided in this study constrain the onset of the Vivero fault between 314 ± 2 and 292 ± 2 Ma and the cessation of tectonic activity between 287 ± 3 Ma and c. 269 Ma (Fig. 6).

An attempt to constrain the minimum duration of the Vivero fault

In the case of Penedo Gordo massif (sample DGP-04), there are two concordant age groups with a difference in age of c. 11 ± 4 Ma. As stated in the results section, the older zircon group with a concordia age at 303 ± 2 Ma cannot correspond to zircon xenocrysts (i.e., unrelated to the magma system) but antecrysts (Charlier et al. 2005; Miller et al. 2007). This suggests that the zircon crystals belonging to the older group represent zircons crystallized from an early magmatic chamber which were incorporated in a later magmatic pulse represented by the youngest zircon population at 292 ± 2 Ma. Examples of this kind of behavior have been demonstrated in previous studies such as Coleman et al. (2004), Paterson et al. (2008) or Díaz Alvarado et al. (2013). Additionally, it is very interesting to note that in the granitoids that surround the Penedo Gordo massif—we refer to samples 05 and 06—zircon grains yielded only Permian dates similar to those obtained in the younger group belonging to the Penedo Gordo massif. This suggests that the early magmatic chamber was local and uniquely related to the intrusion of Penedo Gordo granite and not connected with a large regional magmatic chamber. According to this, we think that the Vivero fault was already active when the early Penedo Gordo magmatic chamber was formed. This hypothesis is further supported by the evidence that at 303 ± 2 Ma, at least one of the regional extensional shear zones within the NW of Iberian massif, the Chandoiro fault, was already active. This fault, located about 40 km to the south of Viveiro fault (see Fig. 1), shows a related granite whose emplacement is interpreted as contemporaneous to its activity (the Veiga massif; Román-Berdiel et al. 1995), with a concordia U–Pb age recently established at 302 ± 3 Ma (Gutiérrez-Alonso et al. 2011). In consequence, the minimum duration of faulting spans between 303 ± 2 and 287 ± 3 Ma, which extends the minimum duration of the Vivero fault to 16 ± 5 Ma (Fig. 6).

Shear strain rate constraints

In the northern segment of the Vivero fault, Martínez et al. (1996) estimated by mineral thermobarometry methods a minimum pressure difference of 150 MPa between the footwall and the hanging wall rocks. Assuming an average rock density (ρ) of $\rho \approx 2,700 \text{ kg m}^{-3}$ and gravitational acceleration (g) $g \approx 9.8 \text{ ms}^{-2}$, a minimum vertical throw of 5.67 km can be deduced. With a fault dip of 60° and a

Table 6 LA-ICP-MS U-Th-Pb data (sample DCP-08) for zircon from the boudinaged granite dykes (Portomarín)

Sample ^a	U (ppm)	Th (ppm)	Th/U	Corrected ratios				$^{208}\text{Pb}/^{232}\text{Th}$ ^b	$\pm 1\text{ s}^{\text{e}}$	% disc.			
				$^{207}\text{Pb}/^{206}\text{Pb}$ ^b	$\pm 1\text{ s}^{\text{e}}$	$^{207}\text{Pb}/^{235}\text{U}$ ^b	$\pm 1\text{ s}^{\text{e}}$						
Zircon_8	5,178	300	0.05	0.07591	0.00648	0.20839	0.01918	0.00023	0.560	0.00599	0.00167	34	
Zircon_2	8,818	2,645	0.27	0.08842	0.00436	0.30678	0.01834	0.0043	0.850	0.00744	0.00019	41	
Zircon_27	3,556	73	0.02	0.06446	0.00417	0.23791	0.01664	0.0027	0.660	0.00820	0.00461	22	
Zircon_20	7,449	190	0.02	0.05935	0.00366	0.23036	0.01503	0.0035	0.320	0.00870	0.00073	15	
Zircon_3	13,527	946	0.06	0.05682	0.00274	0.22557	0.01157	0.0023	0.380	0.00895	0.00043	12	
Zircon_5	5,073	204	0.04	0.15490	0.00201	0.64412	0.01097	0.03023	0.650	0.25307	0.01164	62	
Zircon_4	4,163	76	0.02	0.06019	0.00211	0.26997	0.01033	0.03253	0.560	0.01004	0.00250	15	
Zircon_7	7,634	109	0.01	0.05470	0.00163	0.24457	0.00897	0.03243	0.0046	0.780	0.01012	0.00190	7
Zircon_13	28,273	997	0.03	0.05909	0.00196	0.28373	0.01049	0.03483	0.00943	0.440	0.01078	0.00046	13
Zircon_25	4,813	124	0.02	0.05671	0.00366	0.27864	0.01935	0.03563	0.0042	0.460	0.01108	0.00163	10
Zircon_9	3,000	51	0.02	0.05529	0.00166	0.27138	0.00950	0.03560	0.0044	0.660	0.01110	0.00129	7
Zircon_39	6,321	249	0.04	0.05662	0.00130	0.29142	0.00873	0.03733	0.0056	0.730	0.01161	0.00032	9
Zircon_18	7,475	812	0.10	0.08013	0.00104	0.42645	0.01316	0.03959	0.0111	0.910	0.06455	0.00839	31
Zircon_24	4,761	150	0.03	0.05612	0.00124	0.31328	0.00855	0.04049	0.00049	0.680	0.01260	0.00052	8
Zircon_26	11,187	231	0.02	0.05300	0.00186	0.29860	0.01254	0.04086	0.0069	0.650	0.01281	0.00085	3
Zircon_28	5,492	244	0.04	0.10910	0.00196	0.65324	0.01336	0.04324	0.0042	0.480	0.21477	0.00988	46
Zircon_21	4,016	338	0.08	0.12633	0.00227	0.76303	0.01942	0.04320	0.0078	0.710	0.33817	0.02367	53
Zircon_30	14,4381	4,492	0.03	0.05148	0.00052	0.31325	0.00529	0.04413	0.0052	0.800	0.01388	0.00017	0
Zircon_34	6,305	342	0.05	0.06173	0.00080	0.38294	0.00677	0.04476	0.0054	0.680	0.04316	0.00350	14
Zircon_32	3,426	363	0.10	0.08150	0.00220	0.50395	0.01412	0.04550	0.0034	0.270	0.06524	0.00313	31
Zircon_17	13,6830	4,486	0.03	0.05166	0.00067	0.33249	0.01174	0.04668	0.00133	0.940	0.01468	0.00042	-1
Zircon_31	4,077	146	0.03	0.05740	0.00075	0.37126	0.00709	0.04705	0.0066	0.730	0.03902	0.00429	8
Zircon_33	83,559	1,908	0.02	0.05463	0.00054	0.35962	0.00932	0.04808	0.0115	0.920	0.03348	0.00097	3
Sample ^a													
Sample ^a				U (ppm)	Th (ppm)	Th/U	Corrected ages (Ma)	$^{206}\text{Pb}/^{238}\text{U}$ ^d	$\pm 1\text{ s}^{\text{e}}$	$^{207}\text{Pb}/^{235}\text{U}$ ^d	$\pm 1\text{ s}^{\text{e}}$		
										$^{208}\text{Pb}/^{232}\text{Th}$ ^d	$\pm 1\text{ s}^{\text{e}}$		
Zircon_8	5,178	300	0.05	127	1	192	16	1,093	172	121	34	127	1
Zircon_2	8,818	2645	0.27	160	3	272	14	1,392	94	150	4	160	3
Zircon_27	3,556	73	0.02	170	2	217	14	757	137	165	93	170	2
Zircon_20	7,449	190	0.02	179	2	210	12	580	134	175	15	179	2
Zircon_3	13,527	946	0.06	183	1	207	10	485	106	180	9	183	1
Zircon_5	5,073	204	0.04	192	2	505	7	2,401	22	4,560	188	192	2
Zircon_4	4,163	76	0.02	206	2	243	8	610	75	202	50	206	2
Zircon_7	7,634	109	0.01	206	3	222	7	400	67	204	38	206	3

Table 6 continued

Sample ^a	U (ppm)	Th (ppm)	Th/U	Corrected ages (Ma)						$\pm 1\text{ s}$			
				$^{206}\text{Pb}/^{238}\text{U}^{\text{d}}$	$\pm 1\text{ s}^{\text{e}}$	$^{207}\text{Pb}/^{235}\text{U}^{\text{d}}$	$\pm 1\text{ s}^{\text{e}}$	$^{207}\text{Pb}/^{206}\text{Pb}^{\text{d}}$	$\pm 1\text{ s}^{\text{e}}$				
Zircon_13	28,273	997	0.03	221	3	254	8	570	72	217	9	221	3
Zircon_25	4813	124	0.02	226	3	250	15	480	143	223	33	226	3
Zircon_9	3,000	51	0.02	226	3	244	8	424	67	223	26	226	3
Zircon_39	6,321	249	0.04	236	3	260	7	477	51	233	6	236	3
Zircon_18	7,475	812	0.10	250	7	361	9	1,200	25	1,264	159	250	7
Zircon_24	4,761	150	0.03	256	3	277	7	457	49	253	10	256	3
Zircon_26	11,187	231	0.02	258	4	265	10	329	79	257	17	258	4
Zircon_28	5,492	244	0.04	273	3	510	8	1,784	33	3,932	164	273	3
Zircon_21	4,016	338	0.08	273	5	576	11	2,048	32	5,888	358	273	5
Zircon_30	144,381	4492	0.03	278	3	277	4	262	23	279	3	278	3
Zircon_34	6,305	342	0.05	282	3	329	5	665	28	854	68	282	3
Zircon_32	3,426	363	0.10	287	2	414	10	1,234	53	1,277	59	287	2
Zircon_17	136,830	4486	0.03	294	8	291	9	270	30	294	8	294	8
Zircon_31	4,077	146	0.03	296	4	321	5	507	29	774	83	296	4
Zircon_33	83,559	1908	0.02	303	7	312	7	397	22	666	19	303	7

^a Samples analyzed July 2010 on the LEI-UNAM LA-ICP-MS^b Isotopic ratios are corrected relative to Piešťovice standard zircon (Sláma et al. 2008)^c Rho is the correlation error between errors in the $^{207}\text{Pb}/^{235}\text{U}$ and $^{206}\text{Pb}/^{238}\text{U}$ ratio^d Radiogenic ratios, corrected for common Pb using the ^{204}Pb -correction method, based on the Stacey and Kramers (1975) model^e 1-Sigma errors

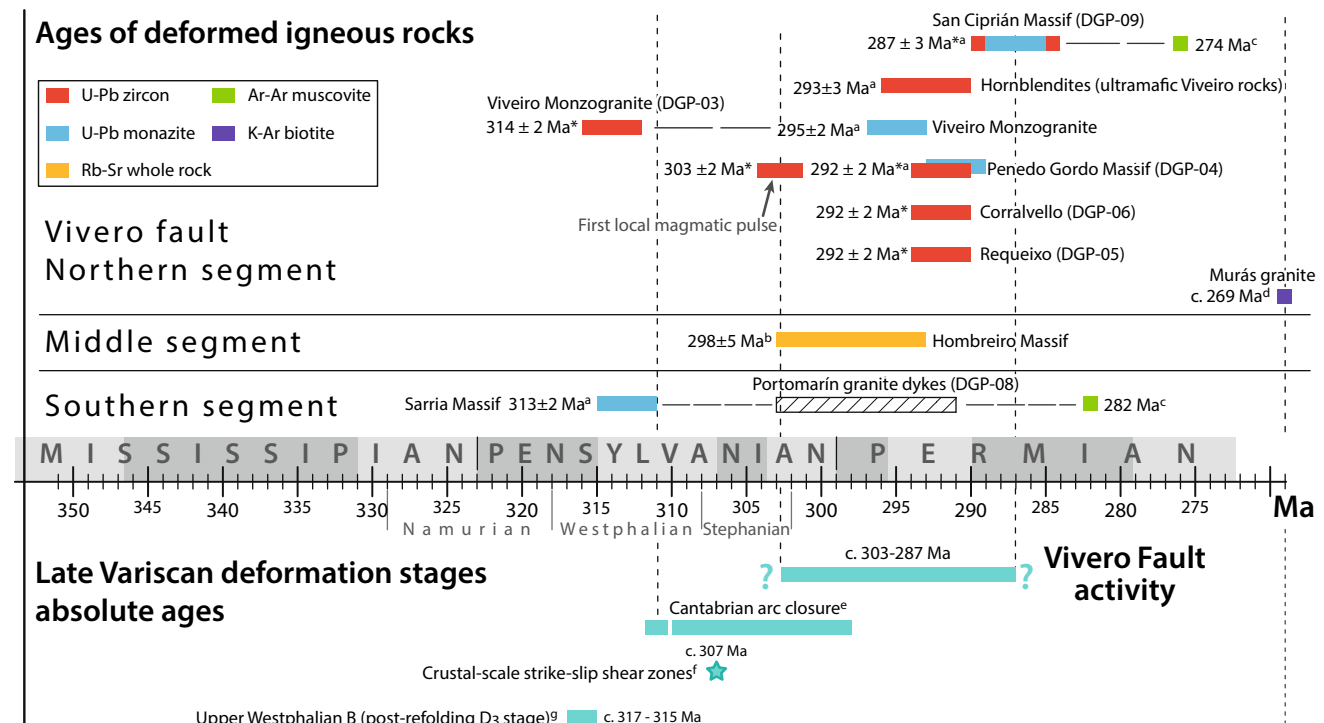


Fig. 6 Timing of emplacement of deformed igneous rocks, the tectonic activity at the Vivero fault and the late Variscan deformation stages in the Iberian massif. Based on our own data (*) and the following references: Fernández-Suárez et al. (2000)^a, Santos Zalduegui et al. (1996)^b, Dallmeyer et al. (1997)^c, Ries (1979)^d, Merino-Tomé

et al. (2009), Weil et al. (2010)^e, Rodríguez et al. (2003), Gutiérrez-Alonso et al. (2010)^f, Colchen (1974)^g. Global stages are based on the International Stratigraphic Chart v2013/01. Western Europe stages based on Richards (2013)

pure dip-slip movement, this results a minimum displacement of 6.55 km (López-Sánchez 2013). On the other hand, according to geothermobarometry calculations by Reche et al. (1998a, b), the garnets in the footwall rocks record a maximum decompression of about 400 MPa, which implies a maximum vertical uplift for the Lugo Dome of about 17 km; this is a maximum movement of 19.63 km along the fault plane assuming all uplift is accommodated along the Vivero fault (Fig. 1c).

If we assume that the displacement across the fault zone is accommodated by deformation distributed linearly, the average rate of finite shear strain can be calculated following (Twiss and Moores 2007):

$$\varepsilon = (0.5(\Delta u/\Delta t)/L)$$

where $\Delta u/\Delta t$ is the displacement rate and L the thickness of the shear zone. Thus, assuming a minimum period of tectonic activity along the Vivero fault in the range of 11–21 Ma (see “An attempt to constrain the minimum duration of the Vivero fault” section) and a shear zone thickness between 300 m (Aranguren and Tubía 1992) to 2,000 m (López-Sánchez 2007, 2013), we obtain a minimum average finite shear strain rate in the range of 9.43×10^{-14} – $2.47 \times 10^{-15} \text{ s}^{-1}$. These average rates fall within the typical

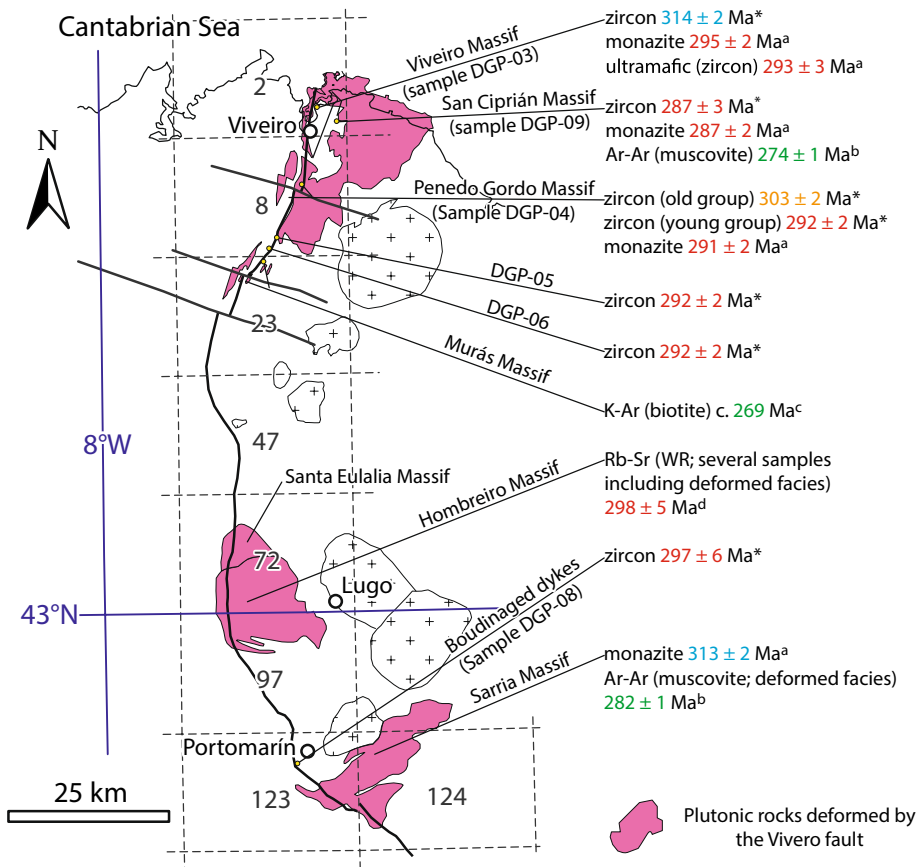
range of natural strain rates (Twiss and Moores 2007), but are at least an order of magnitude faster than the average rates in active normal faults obtained by long-term studies, around 10^{-16} s^{-1} (Nicol et al. 1997; Mouslopoulou et al. 2009). In the event that the tectonic activity along the Vivero fault was longer, strain rates would shift to lower rates than those calculated here.

Implications for the evolution of the Variscan orogeny in the NW of Iberian massif

The timing established for the Vivero fault in this study indicates that the onset of tectonic activity was subsequent to the main Variscan deformation phases established in the NW of the Iberian massif (Fig. 6). This is consistent with the observations made by Matte (1968) and others after him, based on the superposition of tectonic foliations in hanging wall rocks of the fault. Although the precise age of the onset of Vivero fault is unknown, it was post-D3 (i.e., later than Upper Westphalian B, c. 315 Ma) and after the emplacement of the Vivero monzogranite at 314 ± 2 Ma.

Available and scattered radiometric ages constrain strike-slip movements in the NW of the Iberian massif to around 307 Ma (Rodríguez et al. 2003; Gutiérrez-Alonso

Fig. 7 Simplified geological map showing the Vivero fault and the ages available in the plutonic rocks deformed by the fault: *this study; Fernández-Suárez et al. (2000)^a, Dallmeyer et al. (1997)^b, Ries (1979)^c, Santos Zalduegui et al. (1996)^d



et al. 2010) or even later, 290 Ma along the Valdoviño fault (Ortega Cuesta 1988). This implies that most, if not all, strike-slip structures in NW of the Iberian massif are previous to the development of the Vivero fault. Current available radiometric data indicate some overlapping between the Vivero and the Valdoviño faults, as previously proposed by Martínez et al. (1996), although there are significant caveats in the age obtained for the Valdoviño fault, based on K–Ar in deformed granite facies associated with the Valdoviño fault.

The Early Permian age setting for the hanging wall syntectonic thermal metamorphism with andalusite and biotite in the northern segment of the fault precludes the hypothesis portrayed in Arenas and Martínez Catalán (2003), Martínez Catalán et al. (2003) and later Alcock et al. (2009). These authors interpreted the growth of andalusite in relation to the development of a previous (i.e., Namurian–Wesphalian) low-dipping extensional shear zone later overprinted by the Vivero fault.

Tectonic significance of the Vivero fault in the evolution of the orogenic belt

The general features of the Vivero fault show that: (1) it follows approximately the general trend of the Variscan

orogen with an extension direction normal to it and with the sense of shear of top toward the hinterland; (2) its age is roughly Late Carboniferous–Early Permian; and (3) it is located on the margin of a metamorphic dome, the Lugo Dome (Capdevila 1969). These structural features are similar to other Late Carboniferous–Early Permian extensional shear zones described in the French Variscan massifs (Faure 1995; Poilvet et al. 2011; Pitra et al. 2012) (Fig. 8).

One of the consequences of the structural and geochronological data provided in this study is that the extension direction related with the Late Carboniferous–Early Permian shear zones is not constant along the Ibero-Armorican Arc, but remains consistently perpendicular to the general trend of the belt (Fig. 8). At first glance, there are two simple ways to interpret the arrangement of lineations of these Late Carboniferous–Early Permian extensional structures along the Variscan massifs: (1) the extensional faults/shear zones were developed before the closure of the Ibero-Armorican Arc and folded by it; or (2) the extensional faults/shear zones developed once the Ibero-Armorican Arc was formed using the previous Variscan structure, and therefore generated radially outward of the core of the arc.

According to the study of abundant paleomagnetic data (Weil et al. 2010), the Early Permian times mark the termination of the closure of the Cantabrian–Asturian Arc,

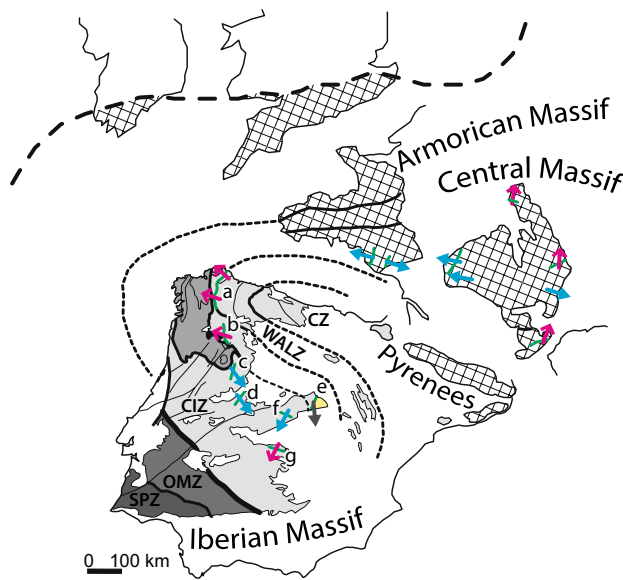


Fig. 8 Simplified structural map of the Ibero-Armorican Arc showing the main extensional shear zones in the French and Iberian Variscan massifs. Green lines represent the approximate orientation of extensional shear zones along the Variscan belt. The arrows indicate the hanging wall extension direction. In blue, pre-D3 (Visean–Namurian–Westphalian) extensional shear zones. In gray, extensional shear zones considered as pre- and/or post-D3. In magenta, Late Carboniferous–Early Permian shear zones. *a* Vivero fault; *b* Chandoiro fault (Iglesias Ponce de León and Varea Nieto 1982; Román-Berdiel et al. 1995; Arias et al. 2002); *c* Tormes extensional shear zone (Escuder Viruete et al. 1994; Escuder Viruete 1998); *d* Salamanca Detachment Zone (Díez Balda et al. 1995); *e* Berzosa-Riaza fault/shear zone (Macaya et al. 1991; Escuder Viruete et al. 1998); *f* Santa María de la Alameda shear zone (Martín-González 2007); *g* Toledo shear zone (Hernández Enrile 1991; Bea et al. 2006). Shear zones in the French massifs based on Faure (1995), Poilvet et al. (2011) and Pitra et al. (2012).

the core of the Ibero-Armorican Arc. This is supported by independent dating of synsedimentary record (Merino-Tomé et al. 2009), although the interpretation of the sedimentary record is not unique. According to Weil and Gutierrez-Alonso and coauthors, arc formation and development occurred between c. 310 and 300 Ma, followed by the generation of magmatism between c. 300 and 292 Ma (Gutiérrez-Alonso et al. 2011; Weil et al. 2013). The available radiometric ages for the Vivero fault would indicate an early coetaneous tectonic activity and the fault outlasting the closure of the arc (Fig. 6). In other words, the arc was formed and closed before the Vivero fault ceased its extensional activity. In fact, a similar geometrical time relation could be said about extensional structures in the French massif, since they all seem to outlast arc closure (Fig. 8). In all cases, radial extension outward from the core of the arc was subsequent to arc closure. Overall, they indicate that the core of the arc was being uplifted with respect to the outer part of the arc, the hinterlands. This suggests that the

external parts of the orogen were substantially thicker than the hinterlands, in disagreement with the limited amount of granitic rocks found at the core. It also fails to explain why an uplifting core of the arc would preserve structures formed at shallow depth at the front of the fold-and-thrust belt (such as submarine slides at the front of moving thrust sheet: see Alonso et al. 2006).

As a final point, it has recently been considered that the role played by the extensional structures in the emplacement of Late Carboniferous–Early Permian magmatism (the so-called post-orogenic magmatism) in the Iberian massif was minor or absent (Gutiérrez-Alonso et al. 2011). In contrast to this, our data clearly indicate a spatial and temporal coincidence between the Vivero fault and the magmatism in this part of the Ibero-Armorican Arc. Furthermore, recently published studies have shown similar Early Permian ages in granites emplaced during the development of extensional detachments in the French Massif Central (Poilvet et al. 2011; Pitra et al. 2012).

Conclusions

The Vivero fault, a regional-scale extensional shear zone located in NW of Iberian massif that runs sub-parallel to the orogen grain showing a consistent movement toward the hinterland (top-to-the-West), was at least active between 303 ± 2 and 287 ± 3 Ma (i.e., Late Carboniferous–Early Permian). Its onset was later than 314 ± 2 Ma. Structural and geochronologic data clearly indicates that the complete development of the Vivero fault was subsequent to the main Variscan deformation phases (namely D₁, D₂ and D₃) in the NW of the Iberian massif.

The minimum time activity and the displacement of the Vivero fault estimated in the northern segment of the fault indicates an average finite shear strain rate in the range of 9.43×10^{-14} – $2.47 \times 10^{-15} \text{ s}^{-1}$.

The ages obtained indicate that in the northern segment of the Vivero fault the metamorphic climax was reached at c. 292 Ma. This is also the age of the local hanging wall high-*T* low-*P* metamorphism developed during the activity of the fault. Our data and observations preclude the hypothesis of the Vivero fault overprinted by a previous extensional high-*T* extensional shear zone as proposed by Arenas and Martínez Catalán (2003), Martínez Catalán et al. (2003) and Alcock et al. (2009).

The extension direction of the Late Carboniferous–Early Permian crustal-scale extensional shear zones along the Ibero-Armorican Arc remains consistently perpendicular to the general curved trend of the belt. The ages available imply that the Vivero fault outlasts the closure of the arc, although also registered an early coetaneous tectonic

activity. Synchronous extensional structures in French and Iberian massifs indicate movement of the hanging wall away from the core of the arc.

During the tectonic activity along the Vivero fault (Late Carboniferous–Early Permian), several granitic massifs were intruded along the structure, including the ultramafic mantle-derived rocks that outcrop near Viveiro. This indicates that the Vivero fault facilitated the ascent and accommodation of magmas in the crust and, in a general sense, that the crustal-scale extensional shear zones played a local role in the Late Carboniferous–Early Permian magmatism.

Acknowledgments This work was funded by the Spanish Ministry of Science and Innovation (Grant References: CGL2006-08822, CGL2006-09509, CSD2006-0041 and CGL2010-14890). Marco A. Lopez-Sánchez acknowledges a doctoral fellowship (BP07-120) in the Severo Ochoa Program (FICYT, Principado de Asturias, Spain). We thank J. R. Martínez Catalán, an anonymous reviewer and editor Soumyajit Mukherjee for insightful comments and suggestions that greatly improved this manuscript.

References

- Alcock JE, Martínez Catalán JR, Arenas R, Díez Montes A (2009) Use of thermal modeling to assess the tectono-metamorphic history of the Lugo and Sanabria gneiss domes, Northwest Iberia. *Bulletin de la Société Géologique de France* 180:179–197. doi:[10.2113/gssgbull.180.3.179](https://doi.org/10.2113/gssgbull.180.3.179)
- Alonso J, Marcos A, Suárez A (2006) Structure and organization of the Porma Melange: progressive denudation of a submarine nappe toe by gravitational collapse. *Am J Sci* 306:32–65. doi:[10.2475/ajs.306.1.32](https://doi.org/10.2475/ajs.306.1.32)
- Andersen T (2002) Correction of common lead in U–Pb analyses that do not report ^{204}Pb . *Chem Geol* 192:59–79. doi:[10.1016/S0009-2541\(02\)00195-X](https://doi.org/10.1016/S0009-2541(02)00195-X)
- Aranguren A (1994) Estructura y cinemática del emplazamiento de los granitos del Domo de Lugo y del Antiforme del Ollo de Sapo. Serie Nova Terra 10
- Aranguren A, Tubía JM (1992) Structural evidence for the relationship between thrusts, extensional faults and granite intrusions in the Variscan belt of Galicia (Spain). *J Struct Geol* 14:1229–1237. doi:[10.1016/0191-8141\(92\)90072-5](https://doi.org/10.1016/0191-8141(92)90072-5)
- Arenas R, Martínez Catalán JR (2003) Low-P metamorphism following a Barrovian-type evolution. Complex tectonic controls for a common transition, as deduced in the Mondoñedo thrust sheet (NW Iberian massif). *Tectonophysics* 365:143–164. doi:[10.1016/S0040-1951\(03\)00020-9](https://doi.org/10.1016/S0040-1951(03)00020-9)
- Arias D, Farias P, Marcos A (2002) Estratigrafía y estructura del Antiforme del Ollo de Sapo en el área de Viana do Bolo-A Gudiña (Provincia de Orense, NO de España): nuevos datos sobre la posición estratigráfica de la Formación porfiroide Ollo de Sapo. *Trabajos de Geología* 23:9–19
- Bastida F, Pulgar JA (1978) La estructura del manto de Mondoñedo entre Burela y Tapia de Casariego (Costa Cantábrica, NW de España). *Trabajos de Geología* 10:75–159
- Bastida F, Marcos A, Marquínez J et al (1984) Mapa Geológico de España e. 1:200.000. Hoja no 1 (La Coruña). Instituto Geológico y Minero de España, Madrid, España
- Bastida F, Martínez Catalán JR, Pulgar JA (1986) Structural, metamorphic and magmatic history of the Mondoñedo nappe (Hercynian belt, NW Spain). *J Struct Geol* 8:415–430. doi:[10.1016/0191-8141\(86\)90060-X](https://doi.org/10.1016/0191-8141(86)90060-X)
- Bea F, Montero P, González Lodeiro F et al (2006) Zircon thermometry and U–Pb ion-microprobe dating of the gabbros and associated migmatites of the Variscan Toledo-Anatetic Complex, Central Iberia. *J Geol Soc* 163:847–855. doi:[10.1144/0016-76492005-143](https://doi.org/10.1144/0016-76492005-143)
- Beaumont C, Jamieson RA, Nguyen MH, Lee B (2001) Himalayan tectonics explained by extrusion of a low-viscosity crustal channel coupled to focused surface denudation. *Nature* 414:738–742. doi:[10.1038/414738a](https://doi.org/10.1038/414738a)
- Bellido F, Brande JL, Lasala M, Reyes J (1992) Consideraciones petrológicas y cornológicas sobre las rocas graníticas hercínicas de Galicia. *Cadernos do Laboratorio Xeolóxico de Laxe* 17:241–261
- Burchfield BC, Zhiliang C, Hodges KV et al (1992) The South Tibetan detachment system, himalayan orogen: extension contemporaneous with and parallel to shortening in a collisional mountain belt. *Geol Soc Am Spec Pap* 269:1–41
- Burg JP, Van Den Driessche J, Brun JP (1994) Syn- to post-thickening extension in the Variscan Belt of Western Europe: modes and structural consequences. *Geol Fr* 3:33–51
- Capdevila R (1969) Le métamorphisme régional progressif et les granites dans le segmentet hercynien Galice nord orientale (NW l'Espagne). Dissertation, Université de Montpellier, France
- Charlier BLA, Wilson CJN, Lowenstern JB et al (2005) Magma generation at a large, hyperactive silicic volcano (Taupo, New Zealand) revealed by U–Th and U–Pb systematics in zircons. *J Petrol* 46:3–32. doi:[10.1093/petrology/egh060](https://doi.org/10.1093/petrology/egh060)
- Colchen M (1974) Geología de la Sierra de la Demanda. Burgos–Logroño (España). Memorias del Instituto Geológico y Minero de España 8. Madrid
- Coleman DS, Gray W, Glazner AF (2004) Rethinking the emplacement and evolution of zoned plutons: geochronologic evidence for incremental assembly of the Tuolumne Intrusive Suite, California. *Geology* 32:433. doi:[10.1130/G20220.1](https://doi.org/10.1130/G20220.1)
- Dallmeyer RD, Martínez Catalán JR, Arenas R et al (1997) Diachronous Variscan tectonothermal activity in the NW Iberian massif: evidence from $^{40}\text{Ar}/^{39}\text{Ar}$ dating of regional fabrics. *Tectonophysics* 277:307–337. doi:[10.1016/S0040-1951\(97\)00035-8](https://doi.org/10.1016/S0040-1951(97)00035-8)
- Díaz Alvarado J, Fernández C, Castro A, Moreno-Ventas I (2013) SHRIMP U–Pb zircon geochronology and thermal modeling of multilayer granitoid intrusions. *Lithos* 175–176:104–123. doi:[10.1016/j.lithos.2013.05.006](https://doi.org/10.1016/j.lithos.2013.05.006)
- Díez Balda MA, Martínez Catalán JR, Ayarza P (1995) Syn-collisional extensional collapse parallel to the orogenic trend in a domain of steep tectonics: the Salamanca Detachment Zone (Central Iberian Zone, Spain). *J Struct Geol* 17:163–182. doi:[10.1016/0191-8141\(94\)E0042-W](https://doi.org/10.1016/0191-8141(94)E0042-W)
- Doblas M, López-Ruiz J, Oyarzun R et al (1994) Extensional tectonics in the central Iberian Peninsula during the Variscan to Alpine transition. *Tectonophysics* 238:95–116. doi:[10.1016/0040-1951\(94\)90051-5](https://doi.org/10.1016/0040-1951(94)90051-5)
- Escuder Viruete J (1998) Relationships between structural units in the Tormes gneiss dome (NW Iberian massif, Spain): geometry, structure and kinematics of contractional and extensional Variscan deformation. *Geol Rundsch* 87:165–179. doi:[10.1007/s005310050199](https://doi.org/10.1007/s005310050199)
- Escuder Viruete J, Arenas R, Martínez Catalán JR (1994) Tectonothermal evolution associated with Variscan crustal extension in the Tormes Gneiss Dome (NW Salamanca, Iberian massif, Spain). *Tectonophysics* 238:117–138. doi:[10.1016/0040-1951\(94\)90052-3](https://doi.org/10.1016/0040-1951(94)90052-3)
- Escuder Viruete J, Hernández Huerta PP, Valverde Vaquero P et al (1998) Variscan syncollisional extension in the Iberian massif: structural, metamorphic and geochronological evidence from the Somosierra sector of the Sierra de Guadarrama (Central Iberian Zone, Spain). *Tectonophysics* 290:87–109. doi:[10.1016/S0040-1951\(98\)00014-6](https://doi.org/10.1016/S0040-1951(98)00014-6)

- Farias P, Gallastegui G, González Lodeiro F et al (1987) Aportaciones al conocimiento de la litoestratigrafía y estructura de Galicia Central. Memórias da Facultade de Ciencias. Universidade do Porto 1:411–431
- Faure M (1995) Late orogenic carboniferous extensions in the Variscan French Massif Central. *Tectonics* 14:132. doi:[10.1029/94TC02021](https://doi.org/10.1029/94TC02021)
- Fernández-Suárez J, Dunning GR, Jenner GA, Gutiérrez-Alonso G (2000) Variscan collisional magmatism and deformation in NW Iberia: constraints from U–Pb geochronology of granitoids. *J Geol Soc* 157:565–576. doi:[10.1144/jgs.157.3.565](https://doi.org/10.1144/jgs.157.3.565)
- Galán G (1987) Las rocas graníticas del macizo de Vivero en el sector norte (Lugo, NO de España). *Corpus Geologicum Gallaeciae Segunda serie II*. La Coruña
- Galán G, Pin C, Duthou JL (1996) Sr–Nd isotopic record of multi-stage interactions between mantle-derived magmas and crustal components in a collision context: the ultramafic-granitoid association from Vivero (Hercynian belt, NW Spain). *Chem Geol* 131:67–91. doi:[10.1016/0009-2541\(96\)00027-7](https://doi.org/10.1016/0009-2541(96)00027-7)
- Gehrels G, Valencia V, Ruiz J (2008) Enhanced precision, accuracy, efficiency, and spatial resolution of U–Pb ages by laser ablation–multicollector–inductively coupled plasma–mass spectrometry. *Geochem Geophys Geosyst* 9:1–13. doi:[10.1029/2007GC001805](https://doi.org/10.1029/2007GC001805)
- González Clavijo E, Díez Balda MA, Alvarez F (1993) Structural study of a semiductile strike-slip system in the Central Iberian Zone (Variscan Fold Belt, Spain): structural controls on gold deposits. *Geol Rundsch* 82:448–460. doi:[10.1007/BF00212409](https://doi.org/10.1007/BF00212409)
- González Lodeiro F, Hernández Urroz J, Klein E et al (1981) Mapa Geológico de España e. 1:200.000. Hoja no 8 (Lugo). Instituto Geológico y Minero de España, Madrid, España
- Goscombe BD, Passchier CW (2003) Asymmetric boudins as shear sense indicators: an assessment from field data. *J Struct Geol* 25:575–589. doi:[10.1016/S0191-8141\(02\)00045-7](https://doi.org/10.1016/S0191-8141(02)00045-7)
- Gutiérrez-Alonso G, Fernández-Suárez J, Jeffries TE et al (2010) Absolute age ($^{40}\text{Ar}^{39}\text{Ar}$ and U–Pb) constrains on orocline development and related lithospheric delamination in the Iberian Armorican Arc. *e-Terra* 23(4). <http://www.metododirecto.pt/CNG2010/index.php/vol/article/viewFile/486/454>
- Gutiérrez-Alonso G, Fernández-Suárez J, Jeffries TE et al (2011) Diachronous post-orogenic magmatism within a developing orocline in Iberia, European Variscides. *Tectonics*. doi:[10.1029/2010TC002845](https://doi.org/10.1029/2010TC002845)
- Hernández Enrile JL (1991) Extensional tectonics of the Toledo ductile-brittle shear zone, Central Iberian Massif. *Tectonophysics* 191:311–324. doi:[10.1016/0040-1951\(91\)90064-Y](https://doi.org/10.1016/0040-1951(91)90064-Y)
- Horn I, Günter D (2003) The influence of ablation carrier gasses Ar, He, and Ne on the particle size distribution and transport efficiencies of laser ablation-induced aerosols: implications for LA-ICP-MS. *Appl Surf Sci* 207:144–157. doi:[10.1016/S0169-4332\(02\)01324-7](https://doi.org/10.1016/S0169-4332(02)01324-7)
- Iglesias Ponce de León M, Varea Nieto R (1982) Mapa geológico de España, scale 1:50.000, 2nd series, no. 228, Viana del Bollo. Madrid, Instituto Geológico y Minero de España, p 26, 1 fold map
- Jackson S, Longerich H, Dunning R, Fryer B (1992) The application of laser-ablation microprobe-inductively coupled plasma mass spectrometry LAM-ICP-MS to *in situ* trace element determinations in minerals. *Can Mineral* 30:1049–1064
- Julivert M, Marcos A (1973) Superimposed folding under flexural conditions in the Cantabrian Zone (Hercynian Cordillera, northwest Spain). *Am J Sci* 273:353–375. doi:[10.2475/ajs.273.5.353](https://doi.org/10.2475/ajs.273.5.353)
- Julivert M, Fontboté J, Ribeiro A, Conde I (1972) Mapa tectónico de la Península Ibérica y Baleares. Instituto Geológico y Minero de España, Madrid, pp 246–265
- Kruhl JH (1996) Prism- and basal-plane parallel subgrain boundaries in quartz: a microstructural geothermobarometer. *J Metamorph Geol* 14:581–589. doi:[10.1046/j.1525-1314.1996.00413.x](https://doi.org/10.1046/j.1525-1314.1996.00413.x)
- Llana-Fúnez S, Marcos A (2001) The Malpica–Lamego Line: a major crustal-scale shear zone in the Variscan belt of Iberia. *J Struct Geol* 23:1015–1030. doi:[10.1016/S0191-8141\(00\)00173-5](https://doi.org/10.1016/S0191-8141(00)00173-5)
- Llana-Fúnez S, Marcos A (2002) Structural record during exhumation and emplacement of high-pressure-low-to intermediate-temperature rocks in the Malpica-Tui unit (Variscan Belt of Iberia). *Geol Soc Am Spec Pap* 364:125–142. doi:[10.1130/0-8137-2364-7.125](https://doi.org/10.1130/0-8137-2364-7.125)
- Llana-Fúnez S, Marcos A (2007) Convergence in a thermally softened thick crust: Variscan intracontinental tectonics in Iberian plate rocks. *Terra Nova* 19:393–400. doi:[10.1111/j.1365-3121.2007.00763.x](https://doi.org/10.1111/j.1365-3121.2007.00763.x)
- López-Sánchez MA (2013) Análisis tectónico de la Falla de Vivero (Galicia, NO de España). Dissertation, Universidad de Oviedo, España. <http://hdl.handle.net/10651/20282>
- López-Sánchez MA (2007) Estudio geológico de la falla de Vivero y estructuras asociadas en la región de Guntín (Lugo, NO de la Península Ibérica). *Trabajos de Geología* 27:97–157
- Lotze F (1945) Zur Gliederung der Varisziden der Iberischen Meseta. *Geotekton Forsch* 6:78–92
- Ludwig KR (2012) Isoplot 3.75: a geochronological toolkit for Microsoft Excel. Berkeley Geochronology Center Special Publication No. 5
- Macaya J, González Lodeiro F, Martínez Catalán JR, Alvarez F (1991) Continuous deformation, ductile thrusting and backfolding of cover and basement in the Sierra de Guadarrama, Hercynian orogen of central Spain. *Tectonophysics* 191:291–309. doi:[10.1016/0040-1951\(91\)90063-X](https://doi.org/10.1016/0040-1951(91)90063-X)
- Marcos A (1971) Cabalgamientos y estructuras menores asociadas originados en el transcurso de una nueva fase hercíniana de deformación en el occidente de Asturias (NW de España). *Breviora Geol Asturica* 15:59–64
- Marcos A (1973) Las series del Paleozoico Inferior y la estructura hercíniana del occidente de Asturias (NW de España). *Trabajos de Geología* 6:3–107
- Martínez Catalán JR (1983) Deformación heterogénea en los macizos graníticos de Sarria y Santa Eulalia de Pena (provincia de Lugo). *Studia Geologica Salmanticensia* 18:39–64
- Martínez Catalán JR (1985) Estratigrafía y estructura del Domo de Lugo (Sector Oeste de la zona Asturooccidental-leonesa. *Corpus Geologicum Gallaeciae Segunda serie II*, La Coruña
- Martínez Catalán JR, Arenas R, Díez Balda MA (2003) Large extensional structures developed during emplacement of a crystalline thrust sheet: the Mondoñedo nappe (NW Spain). *J Struct Geol* 25:1815–1839. doi:[10.1016/S0191-8141\(03\)00038-5](https://doi.org/10.1016/S0191-8141(03)00038-5)
- Martínez Catalán JR, Arenas R, Abati J et al (2007) Space and time in the tectonic evolution of the northwestern Iberian massif: implications for the Variscan belt. In: Hatcher Jr RD, Carlson MP, McBride JH, Martínez Catalán JR (eds), 4-D framework of continental crust. *Geol Soc Am Memoir* 200:403–423. doi:[10.1130/2007.1200\(21\)](https://doi.org/10.1130/2007.1200(21))
- Martínez FJ, Rölet J (1988) Late Palaeozoic metamorphism in the northwestern Iberian Peninsula, Brittany and related areas in SW Europe. *Geol Soc Lond Spec Publ* 38:611–620. doi:[10.1144/GSL.SP.1988.038.01.42](https://doi.org/10.1144/GSL.SP.1988.038.01.42)
- Martínez FJ, Julivert M, Sebastian A et al (1988) Structural and thermal evolution of high-grade areas in the northwestern parts of the Iberian massif. *Am J Sci* 288:969–996. doi:[10.2475/ajs.288.10.969](https://doi.org/10.2475/ajs.288.10.969)
- Martínez FJ, Carreras J, Arboleya ML, Dietsch C (1996) Structural and metamorphic evidence of local extension along the Vivero fault coeval with bulk crustal shortening in the Variscan chain (NW Spain). *J Struct Geol* 18:61–73. doi:[10.1016/0191-8141\(95\)00080-W](https://doi.org/10.1016/0191-8141(95)00080-W)
- Martínez FJ, Reche J, Arboleya ML (2001) P–T modelling of the andalusite–kyanite–andalusite sequence and related assemblages in high-Al graphitic pelites. Prograde and retrograde paths in a late kyanite belt in the Variscan Iberia. *J Metamorph Geol* 19:661–677. doi:[10.1046/j.0263-4929.2001.00335.x](https://doi.org/10.1046/j.0263-4929.2001.00335.x)

- Martín-González F (2007) Evolution of an extensional shear zone in retrograde metamorphic conditions in the Iberian massif: Santa María de la Alameda shear zone (Spanish Central System). *Cadernos do Laboratorio Xeolóxico de Laxe* 32:63–81
- Matte P (1968) La structure de la virgation hercynienne de Galice (Espagne). *Geol Alp* 44:155–280
- Matte P (1986) Tectonics and plate tectonics model for the Variscan belt of Europe. *Tectonophysics* 126:329–374. doi:[10.1016/0040-1951\(86\)90237-4](https://doi.org/10.1016/0040-1951(86)90237-4)
- Matte P, Ribeiro A (1975) Forme et réorientation de l'ellipsoïde de déformation dans la virgation hercynienne de Galice. Relations avec le plissement et hypothèses sur la genèse de l'arc ibéro-armoricain. *Comptes Rendus Académie Des Sciences Paris* 280:2825–2828
- Merino-Tomé OA, Bahamonde JR, Colmenero JR et al (2009) Emplacement of the Cuera and Picos de Europa imbricate system at the core of the Iberian–Armoricane arc (Cantabrian zone, north Spain): new precisions concerning the timing of arc closure. *Geol Soc Am Bull* 121:729–751. doi:[10.1130/B26366.1](https://doi.org/10.1130/B26366.1)
- Miller JS, Matzel JEP, Miller CF et al (2007) Zircon growth and recycling during the assembly of large, composite arc plutons. *J Volcanol Geotherm Res* 167:282–299. doi:[10.1016/j.jvolgeores.2007.04.019](https://doi.org/10.1016/j.jvolgeores.2007.04.019)
- Mouslopoulou V, Walsh JJ, Nicol A (2009) Fault displacement rates on a range of timescales. *Earth Planet Sci Lett* 278:186–197. doi:[10.1016/j.epsl.2008.11.031](https://doi.org/10.1016/j.epsl.2008.11.031)
- Mukherjee S (2013a) Channel flow extrusion model to constrain dynamic viscosity and Prandtl number of the Higher Himalayan Shear Zone. *Int J Earth Sci* 102:1811–1835. doi:[10.1007/s00531-012-0861-z](https://doi.org/10.1007/s00531-012-0861-z)
- Mukherjee S (2013b) Higher Himalaya in the Bhagirathi section (NW Himalaya, India): its structures, backthrusts and extrusion mechanism by both channel flow and critical taper mechanisms. *Int J Earth Sci* 102:1851–1870. doi:[10.1007/s00531-012-0861-z](https://doi.org/10.1007/s00531-012-0861-z)
- Mukherjee S, Koyi HA (2010a) Higher Himalayan Shear Zone, Sutlej section: structural geology and extrusion mechanism by various combinations of simple shear, pure shear and channel flow in shifting modes. *Int J Earth Sci* 99:1267–1303. doi:[10.1007/s00531-009-0458](https://doi.org/10.1007/s00531-009-0458)
- Mukherjee S, Koyi HA (2010b) Higher Himalayan Shear Zone, Zanskar Indian Himalaya: microstructural studies and extrusion mechanism by a combination of simple shear and channel flow. *Int J Earth Sci* 99:1083–1110. doi:[10.1007/s00531-009-0447-z](https://doi.org/10.1007/s00531-009-0447-z)
- Mukherjee S, Mukherjee B, Thiede R (2013) Geosciences of the Himalaya–Karakoram–Tibet orogen. *Int J Earth Sci* 102:1757–1758. doi:[10.1007/s00531-013-0934-0](https://doi.org/10.1007/s00531-013-0934-0)
- Nicol A, Walsh JJ, Watterson J, Underhill J (1997) Displacement rates of normal faults. *Nature* 390:157–159. doi:[10.1038/36548](https://doi.org/10.1038/36548)
- Ortega Cuesta LA (1988) Estudio petrogenético del granito sincinético de dos micas de A Espenuca (A Coruña). Serie Nova Terra, Laboratorio Xeolóxico de Laxe 14:1–377
- Ortega LA, Aranguren A, Menéndez M, Gil Ibarguchi I (2000) Petrogenésis, edad y emplazamiento del granito tardí-hercínico de Veiga (antiforme del Ollo de Sapo, Noroeste de España). *Cadernos do Laboratorio Xeolóxico de Laxe* 25:265–268
- Pamplona J, Rodrigues BC (2010) Kinematic interpretation of shearband boudins: New parameters and ratios useful in HT simple shear zones. *J Struct Geol* 33:38–50. doi:[10.1016/j.jsg.2010.10.004](https://doi.org/10.1016/j.jsg.2010.10.004)
- Parga Pondal I, Matte P, Capdevila R (1964) Introduction à la géologie de l'“Ollo de Sapo”, formation porphyroïde anté-silurienne du Nord-Ouest de l'Espagne. Notas y Comunicaciones del Instituto Geológico y Minero de España 76:119–153
- Parga Pondal I, Matte P, Capdevila R et al (1967) Carte géologique du Nord-ouest de la Peninsule Ibérique (Hercynien et anté-hercynien). e. 1:500.000. Direcção Geral de Minas e Serviços Geológicos de Portugal. Lisboa
- Parga Pondal I, Parga Peinador JR, Vegas R, Marcos A (1982) Mapa Xeolóxico do Macizo Hespérico e. 1:500.000. Publicaciones del Área de Xeoloxía e Minería. Seminario de estudios galegos, Edificio de Castro, A Coruña
- Paterson SR, Tobisch OT (1988) Using pluton ages to date regional deformations: problems with commonly used criteria. *Geology* 16:1108–1111. doi:[10.1130/0091-7613\(1988\)16:11;1-U](https://doi.org/10.1130/0091-7613(1988)16:11;1-U)
- Paterson S, Žák J, Janoušek V (2008) Growth of complex sheeted zones during recycling of older magmatic units into younger: Sawmill Canyon area, Tuolumne batholith, Sierra Nevada, California. *J Volcanol Geotherm Res* 177:457–484. doi:[10.1016/j.jvolgeores.2008.06.024](https://doi.org/10.1016/j.jvolgeores.2008.06.024)
- Pereira MF, Chichorro M, Williams IS et al (2009) Variscan intra-orogenic extensional tectonics in the Ossa-Morena Zone (Évora-Aracena-Lora del Río metamorphic belt, SW Iberian massif): SHRIMP zircon U-Th-Pb geochronology. *Geol Soc Lond Spec Publ* 327:215–237. doi:[10.1144/SP327.11](https://doi.org/10.1144/SP327.11)
- Pérez-Estaún A, Bea F (2004) Macizo Ibérico. In: Vera JA (ed) *Geología de España*. SGE-IGME, Madrid, pp 465–527
- Pérez-Estaún A, Martínez Catalán JR, Bastida F (1991) Crustal thickening and deformation sequence in the footwall to the suture of the Variscan belt of northwest Spain. *Tectonophysics* 191:243–253. doi:[10.1016/0040-1951\(91\)90060-6](https://doi.org/10.1016/0040-1951(91)90060-6)
- Pérez-Estaún A, Bastida F, Alonso JL et al (1988) A thin-skinned tectonics model for an arcuate fold and thrust belt: the Cantabrian Zone (Variscan Ibero-Armorican Arc). *Tectonics* 7:517–537. doi:[10.1029/TC007i003p00517](https://doi.org/10.1029/TC007i003p00517)
- Pitra P, Poujol M, Van Den Driessche J et al (2012) Early Permian extensional shearing of an Ordovician granite: the Saint-Europe ‘C/S-like’ orthogneiss (Montagne Noire, French Massif Central). *CR Geosci* 344:377–384. doi:[10.1016/j.crte.2012.06.002](https://doi.org/10.1016/j.crte.2012.06.002)
- Poilvert JC, Poujol M, Pitra P et al (2011) The Montalet granite, Montagne Noire, France: an Early Permian syn-extensional pluton as evidenced by new U-Th-Pb data on zircon and monazite. *CR Geosci* 343:454–461. doi:[10.1016/j.crte.2011.06.002](https://doi.org/10.1016/j.crte.2011.06.002)
- Ponce Iglesias, de León M, Choukroune P (1980) Shear zones in the Iberian Arc. *J Struct Geol* 2:63–68. doi:[10.1016/0191-8141\(80\)90035-8](https://doi.org/10.1016/0191-8141(80)90035-8)
- Rathore JS, Courrioux G, Choukroune P (1983) Study of ductile shear zones (Galicia, Spain) using texture goniometry and magnetic fabric methods. *Tectonophysics* 98:87–109. doi:[10.1016/0040-1951\(83\)90212-3](https://doi.org/10.1016/0040-1951(83)90212-3)
- Reche J, Martínez FJ, Arboleja ML (1998a) Low- to medium-pressure Variscan metamorphism in Galicia (NW Spain): evolution of a kyanite-bearing synform and associated bounding antiformal domains. *Geol Soc Lond Spec Publ* 138:61–79. doi:[10.1144/GSL.SP.1996.138.01.05](https://doi.org/10.1144/GSL.SP.1996.138.01.05)
- Reche J, Martínez FJ, Arboleja ML et al (1998b) Evolution of a kyanite-bearing belt within a HT-LP orogen: the case of NW Variscan Iberia. *J Metamorph Geol* 16:379–394. doi:[10.1111/j.1525-1314.1998.00142.x](https://doi.org/10.1111/j.1525-1314.1998.00142.x)
- Ribeiro A (1970) Position structural des Massifs de Morais et Bragança (Tras-os-Montes). *Commun Serv Geol Port* 54:115–138
- Richards BC (2013) Current status of the International Carboniferous time scale. In: Lucas SG et al (eds) *The Carboniferous–Permian transition*. N M Mus Natl Hist Sci Bull 60:348–353
- Ries AC (1979) Variscan metamorphism and K–Ar dates in the Variscan fold belt of S Brittany and NW Spain. *J Geol Soc* 136:89–103. doi:[10.1144/gsjgs.136.1.0089](https://doi.org/10.1144/gsjgs.136.1.0089)
- Rodríguez J, Cosca MA, Gil Ibarguchi JI, Dallmeyer RD (2003) Strain partitioning and preservation of $^{40}\text{Ar}/^{39}\text{Ar}$ ages during Variscan exhumation of a subducted crust (Malpica-Tui complex, NW Spain). *Lithos* 70:111–139. doi:[10.1016/S0024-4937\(03\)00095-1](https://doi.org/10.1016/S0024-4937(03)00095-1)
- Román-Berdiel T, Pueyo-Morer EL, Casas-Sainz AM (1995) Granite emplacement during contemporary shortening and normal faulting: structural and magnetic study of the

- Veiga Massif (NW Spain). *J Struct Geol* 17:1689–1706. doi:[10.1016/0191-8141\(95\)00062-I](https://doi.org/10.1016/0191-8141(95)00062-I)
- Rutter EH, Mecklenburgh J, Brodie KH (2011) Rock mechanics constraints on mid-crustal low-viscosity flow beneath Tibet. In: Prior DJ, Rutter EH, Tatham DJ (eds) Deformation mechanisms, rheology and tectonics: microstructures, mechanics and anisotropy. *Geol Soc Lond Spec Publ* 360:329–336. doi:[10.1144/SP360.19](https://doi.org/10.1144/SP360.19)
- Sambridge MS, Compston W (1994) Mixture modeling of multi-component data sets with application to ion-probe zircon ages. *Earth Planet Sci Lett* 128:373–390. doi:[10.1016/0012-821X\(94\)90157-0](https://doi.org/10.1016/0012-821X(94)90157-0)
- Santos Zalduogui JF, Pin C, Aranguren A, Gil-Ibarguchi JI (1996) Application of specific extraction chromatographic methods to the Rb–Sr, Sm–Nd isotope study of geological samples: the Hombreiro-Santa Eulalia Granite (Lugo, NW Spain). *Geogaceta* 20:495–497
- Sláma J, Košler J, Condon DJ et al (2008) Plešovice zircon: a new natural reference material for U–Pb and Hf isotopic microanalysis. *Chem Geol* 249:1–35. doi:[10.1016/j.chemgeo.2007.11.005](https://doi.org/10.1016/j.chemgeo.2007.11.005)
- Solari L, Tanner M (2011) UPb.age, a fast data reduction script for LA-ICP-MS U–Pb geochronology. *Revista Mexicana de Ciencias Geológicas* 28:83–91
- Solari L, Gómez-Tuena A, Bernal J et al (2010) U–Pb zircon geochronology by an integrated LA-ICPMS microanalytical workstation: achievements in precision and accuracy. *Geostand Geanal Res* 34:5–18. doi:[10.1111/j.1751-908X.2009.00027.x](https://doi.org/10.1111/j.1751-908X.2009.00027.x)
- Stacey JS, Kramers JD (1975) Approximation of terrestrial Lead isotope evolution by a two-stage model. *Earth Planet Sci Lett* 26:207–221. doi:[10.1016/0012-821X\(75\)90088-6](https://doi.org/10.1016/0012-821X(75)90088-6)
- Tera F, Wasserburg GJ (1972) U–Th–Pb systematics in three Apollo 14 basalts and the problem of initial Pb in lunar rocks. *Earth Planet Sci Lett* 14:281–304. doi:[10.1016/0012-821X\(72\)90128-8](https://doi.org/10.1016/0012-821X(72)90128-8)
- Twiss RJ, Moores EM (2007) Structural Geology, 2nd edn. W. H. Freeman and Company, New York
- Valverde Vaquero P, Hernández-Huerta PP, Escuder Viruete J, Dunning GR (1995) Comparison of the Precambrian and Paleozoic evolution of the Sierra de Guadarrama (Central Iberian Zone, Spain) and the Gondwanan Margin, Newfoundland Appalachians (GMNA). *Terra Nova* 7:278
- Vegas N, Aranguren A, Tubia J (2001) Granites built by sheeting in a fault stepover (the Sanabria Massifs, Variscan Orogen, NW Spain). *Terra Nova* 13:180–187. doi:[10.1046/j.1365-3121.2001.00343.x](https://doi.org/10.1046/j.1365-3121.2001.00343.x)
- Weil AB, Gutiérrez-Alonso G, Conan J (2010) New time constraints on lithospheric-scale oroclinal bending of the Ibero-Armorican Arc: a palaeomagnetic study of earliest Permian rocks from Iberia. *J Geol Soc* 167:127–143. doi:[10.1144/0016-76492009-002](https://doi.org/10.1144/0016-76492009-002)
- Weil AB, Gutiérrez-Alonso G, Johnston ST, Pastor-Gálán D (2013) Kinematic constraints on buckling a lithospheric-scale orocline along the northern margin of Gondwana: a geologic synthesis. *Tectonophysics* 582:25–49. doi:[10.1016/j.tecto.2012.10.006](https://doi.org/10.1016/j.tecto.2012.10.006)
- Wendt I, Carl C (1991) The statistical distribution of the mean squared weighted deviation. *Chem Geol Isot Geosci Sect* 86:275–285. doi:[10.1016/0168-9622\(91\)90010-T](https://doi.org/10.1016/0168-9622(91)90010-T)
- Wetherill GW (1956) Discordant uranium-lead ages. *Trans Am Geophys Union* 37:320–326
- Yin A (2006) Cenozoic tectonic evolution of the Himalayan orogen as constrained by along-strike variation of structural geometry, exhumation history, and foreland sedimentation. *Earth Sci Rev* 76:1–131. doi:[10.1016/j.earscirev.2005.05.004](https://doi.org/10.1016/j.earscirev.2005.05.004)